Composite Structures 116 (2014) 193–210

Contents lists available at ScienceDirect

Composite Structures

journal homepage: www.elsevier.com/locate/compstruct

Low speed impact of laminated polymethylmethacrylate/adhesive/polycarbonate plates

G.O. Antoine, R.C. Batra *

Department of Engineering Science and Mechanics, M/C 0219, Virginia Polytechnic Institute and State University, Blacksburg, VA 24061, USA

ARTICLE INFO

Article history:
Available online 9 May 2014

Keywords:
Laminates
Impact
Cracks
Damage
Finite elasto-plastic deformations

ABSTRACT

We study three-dimensional finite transient deformations of transparent poly-methyl-methacrylate (PMMA)/adhesive/polycarbonate (PC) laminates impacted at low speed by a hemispherical nosed rigid cylinder using the commercial finite element (FE) software LS-DYNA. The two glassy polymers PMMA and PC are modeled as thermo-elasto-visco-plastic materials by using the constitutive relation proposed by Mulliken and Boyce and modified by Varghese and Batra. For the nearly incompressible viscoelastic bonding layer, the elastic response is modeled by the Ogden relation and the viscous response by the Prony series. Delamination at interfaces between the adhesive and the polymeric sheets is simulated by using the cohesive zone model incorporated in LS-DYNA. The effective plastic strain, the maximum principal stress, and the maximum stretch based failure criteria are used for delineating failure in PC, PMMA and the adhesive, respectively. Failed elements are deleted from the analysis domain. The three layers are discretized by using 8-node brick elements and integrals over elements are numerically evaluated by using a reduced Gauss integration rule. The coupled nonlinear ordinary differential equations obtained by the Galerkin approximation are integrated by using the conditionally stable explicit algorithm. Results have been computed for at least two different FE meshes. The computed number and configurations of cracks in the PMMA are found to qualitatively agree with the test observations. It is also found that the energy dissipated due to plastic deformations in the PC is considerably more than that due to cracks formed in the PMMA.

1. Introduction

Polymers are composed of long chains of monomers while a metal is generally a polycrystalline material. This difference in the microstructure explains why their thermo-mechanical response is quite different. Polymers usually exhibit strong strain-rate dependence in their mechanical response and are widely used as transparent armors because of their high specific impact performance, e.g., see Radin and Goldsmith [1]. Sands et al. [2] have reported that polymethylmetha-acrylate (PMMA) and polycarbonate (PC) polymers have better impact resistance than most glasses. Rabinowitz et al. [3] used a high pressure torsion test to experimentally investigate the effect of pressure on the quasi-static shear stress-shear strain response and on the fracture strain of PMMA and poly(ethylene terephthalate). They found that an increase in the hydrostatic pressure increases the yield strain, the yield stress and the fracture stress of the materials but decreases the fracture strain.

The mechanical behavior of glassy polymers has been experimentally and computationally studied by several investigators. Duckett et al. [4] experimentally studied the strain rate and pressure dependence of the yield stress of PMMA and poly (ethylene terephthalate) deformed in uniaxial compression at strain rates from 10^{-6}/s to 10^{-1}/s. They found that the yield stresses in compression and torsion increase monotonically with increasing strain-rate and decreasing temperature. This was confirmed by Arruda et al. [5] in the same range of strain rates and by Mullliken and Boyce [6] for low to high strain rates (up to 10^3/s). Similar conclusions about the dependence of the yield strain and the yield stress upon the strain rate and the temperature hold for the PC material [6–11]. Moy et al. [8] performed uniaxial compression tests on Lexan 9034A PC from 10^{-4}/s to 4600/s strain rates. They used an Instron test machine for the quasi-static tests and a split-Hopkinson (Kolsky) bar for the high strain rate experiments. Rittel et al. [12] studied heating of PMMA samples subjected to uniaxial compressive cyclic loading at stress levels above the yield stress of the PMMA and at strain rates up to 0.1/s. They related the temperature rise to the chain mobility of the polymers. Rittel [13] and Rittel and Rabinowitz [14] performed uniaxial tensile and

* Corresponding author. Tel.: +1 540 231 6051; fax: +1 540 231 4574.
E-mail addresses: antoineg@ut.edu (G.O. Antoine), rbatra@vt.edu (R.C. Batra).

http://dx.doi.org/10.1016/j.compstruct.2014.04.006
0263-8223/

cyclic tests on PMMA and PC at low strain rates and measured the temperature rise.

Schmachtenberg et al. [15] proposed a method to find values of material parameters for modeling the mechanical behavior of thermoplastics. Arruda et al. [5] performed uniaxial compression tests on PMMA samples at various strain rates and temperatures, and developed a material model for the PMMA based on the multiplicative decomposition of the deformation gradient into elastic, thermal and inelastic parts. Moreover, they assumed that a part of the energy dissipated due to inelastic deformations is converted into heating while the remainder contributes to the back stress. Richeton et al. [9–11] used shift factors for the strain rate and the stresses to model the temperature and strain rate dependence of the yield stress of amorphous polymers. Richeton et al. [16] and Tervoort et al. [17] employed a spring in series with a dashpot and a Langevin spring to derive constitutive equations for polymers. Buckley and Jones [18] modeled the behavior of amorphous polymers near the glass transition temperature by decomposing the stress into two components, a bond stretching stress (partially irreversible) and a reversible conformational stress, and introduced a shift factor for the temperature and the strain rate dependence of the elastic moduli. Alavarado-Contreras et al. [19] used a simple chemical description of the amorphous and the crystalline phases to derive equations describing the mechanical behavior of amorphous semicrystalline materials. An eight-chain model is used for the amorphous phase and the stress tensor for this phase is the sum of a conformational stress tensor and a back-stress tensor. The deformation of the crystalline phase is assumed to be driven by effective shear stresses along its eight slip systems. Furthermore, they introduced two scalar variables that represent damage in each phase, proposed their evolution relations, and considered the loss of stiffness of the material due to progressive damage prior to failure. Boyce et al. [20] and Mulliken and Boyce [6] introduced a rate dependent model for the behavior of glassy polymers that assumes the coexistence of three different phases with the same values of the deformation gradient at a material point. Two of these phases have similar constitutive equations with different values of material parameters, and the third phase contributes to the general stress via a back-stress component. This material model has been generalized by Varghese and Batra [21,22] to account for the dependence of the elastic moduli upon the temperature and temperature dependent strain softening. Predictions from this work for uniaxial tensile and compressive deformations compare well with the test results at low and high strain rates.

The damage initiation and evolution, and the failure of polymers have been studied experimentally and numerically. Lajtai [23] studied the failure of pre-cracked specimens subjected to compressive loading and used a modified Coulomb model to study the final stages of their failure. Saghafi et al. [24] proposed a criterion to predict mode II and mixed-mode fracture toughness of brittle materials. Using data obtained from three-point bend tests on marble specimens they found that their criterion predicted better the failure of specimens than that given by the maximum tangential stress (MTS) criterion. Seweryn [25] proposed a criterion for brittle fracture of structures with sharp notches based on modes I, II and III stress intensity factors. Seweryn and Lukaszewicz [26] analyzed crack initiation in brittle specimens with V-shaped notches under mixed mode loading and found good agreement between the experimental measurements and the J-integral computed with the boundary element method. Vandenberghe et al. [27] proposed a model of crack formation in PMMA plates impacted at normal incidence. They considered energy dissipated due to crack formation and for flexural deformations of petals formed in the cracked plate. They could accurately predict the number of cracks formed in the plate as a function of the impact speed and the plate thickness.

Schultz [28] has related the failure of semicrystalline polymers to the spherulitic structure of the material and the inter- and intraspherulitic fracture. Zaïri et al. [29] proposed constitutive equations to describe the progressive void growth in elasto-viscoplastic polymers, and showed that their model could predict well the stress–strain response of rubber-modified PMMA deformed in uniaxial tension. Ayatollahi et al. [30] performed fracture tests on semi-circular PMMA specimens containing an edge crack and modeled crack propagation using the finite element method (FEM) and the MTS failure criterion. They accurately predicted the crack trajectory in semi-circular bend (SCB) specimens. For small preexisting cracks in an infinite PMMA medium, Beaumont et al. [31] investigated the relation between the crack propagation speed and the stress intensity factor at the crack tip for mode I failure of sharply-notched specimens. Wada et al. [32] experimentally studied the impact fracture toughness of edge-cracked PMMA specimens and computationally analyzed their 3D deformations using the FEM. Marshall et al. [33] introduced a factor to account for the notch size in the calculation of the energy release-rate for the PMMA material, which enabled them to derive a material specific energy/area that is independent of the specimen geometry. In their work the ratio of the initial crack length to the width of the sample ranged between 0.03 and 0.5. Moy et al. [34] found that the failure of PMMA is ductile at strain rates $\ll 1$/s and brittle at strain rates $\gg 1$/s. Weerasooriya et al.'s [35] test data have revealed that the fracture toughness of PMMA for strain rates >100/s is almost twice that for quasi-static loading.

The failure modes of PC are quite different from those of PMMA. Chang and Chu [36] study the effect of temperature and notch-tip radius on the fracture mode of PC and of a modified PC. They found the existence of a semi-ductile fracture mode at low temperatures (-40 °C) for some notch-tip radii and proposed a diagram describing the 2D-fracture mode of PC as a function of the temperature and of the notch-tip radius. Mills [37] performed Charpy impact tests on notched PC bars and studied the effect of annealing on the ductile to brittle failure transitions. Fraser and Ward [38] investigated the effect of the notch-tip radius on the impact fracture behavior of PC samples. Allen et al. [39] measured the Charpy impact strength of notched polydiancarbonate and found that the polymer exists in two different varieties with different yield and failure properties, but did not relate this difference to the morphology of the polymers. Rittel et al. [40] tested cracked specimens and delineated two failure mechanisms, opening and shear banding, in PC as a function of the mode-mixity. Rittel and Levin [41] used two different experimental set-ups to study crack propagation in PC with either mode-I dominant or mode-II dominant deformations. They found that the same mechanisms govern the failure of PC regardless of the mode-mixity. Curran et al. [42] analyzed the fracture of PC disks subjected to dynamic flat-plate impact and predicted the level of damage induced in the PC sample with a damage model based on the nucleation, growth and coalescence of cracks. Plati and Williams [43,44] compared the energy release rate of different polymers including PMMA and PC obtained with Charpy and Izod tests at different temperatures, and found that they gave essentially the same value of the energy release rate. Adams et al. [45] used three-point bend specimens made of five different polymers (PC, polyacetal, two nylons and PMMA) to measure the plane strain fracture toughness of these materials under impact loading. Ogihara et al. [46] examined fracture mechanisms of polymeric materials by high velocity impact and quasistatic perforation tests and compared the static and the dynamic perforation energies of PMMA plates with various edge lengths and thicknesses. Fleck et al. [47] pointed out that craze nucleation was the principal failure mechanism for both PMMA and PC at high strain rates despite PMMA exhibiting brittle failure and PC ductile failure. Livingstone et al. [48] and Richards et al. [49] used a bulk strain based failure criterion to model damage in PC and a principal tensile stress criterion to model the failure of polyurethane interlayer during their simulations of the impact of a glass/interlayer/PC laminate. They accurately simulated the fracture pattern of the impacted plate, and predicted the ballistic limit (v_{50}) within 10% accuracy. Kelly [50] used the Johnson–Holmquist failure criterion to simulate damage in PC and PMMA.

Kihara et al. [51] measured the impact shear strength of adhesive interlayers, and developed an experimental apparatus that can be used to deform an adhesive in shear at high strain rates. They used it in conjunction with the FE simulations to determine the maximum shear stress in the sample at fracture and showed that it equals the impact shear strength.

The study of failure of plates subjected to low speed impact is important for analyzing the survivability of goggles, aircraft canopy and windshields. Tsai and Chen [52] have investigated the fracture of a glass plate impacted by a spherical (deformable or rigid) body. They related the critical stress developed in the plate to the impact velocity, the plate thickness and the support span. They found that the Hertzian fracture (formation of a fracture cone under the impact site) is predominant for short support span and the sample fails due to flexural fracture for large support spans. Fountzoulas et al. [53] used the FEM to investigate the effect of defects on the impact response of aluminate spinel ($MgAl_2O_4$), polyurethane and PC plates. Gilde et al. [54] performed ballistic impact tests on monolithic PMMA plates and on glass/PMMA/PC laminates, and exploited the synergy between glass and polymers to create a lightweight transparent armor with improved ballistic resistance. They showed that the laminated structure rather than a monolithic glass increased the ballistic limit by nearly 50% for the same areal density. In numerical work, the v_{50} of a structure equals the minimum impact speed required to perforate it.

Zee et al. [55] used a gas gun to conduct impact tests on composites made of epoxy matrix reinforced with polyethylene and polyester fibers. They found that the energy loss mechanisms are the fracture of the target and the generation of frictional heat due to the passage of the projectile through the composite. Tarim et al. [56] experimentally studied the ballistic impact performance of polymer-based composites. They performed high velocity (between 180 and 425 m/s, bullets with mass ranging from 3.2 to 15.55 g) impact experiments on composites and showed that adding layers to the structure increases its bending and tensile stiffness and reduces the residual velocity of the bullet for perforated targets.

The low-velocity impact of composite panels is often modeled as quasi-static indentation. Wu and Chang [57] used the finite element method to study the quasi-static impact of a graphite/epoxy sandwich beam with an elasto-plastic foam core. They found that matrix cracking could be predicted by comparing the principal stresses in the matrix with the transverse strength of the lamina and used the strain-energy release rate (SERR) to predict the delamination. Tita et al. [58] studied the low-velocity impact (indentation) response of carbon fiber reinforced epoxy disks by using a user defined subroutine implemented in the FE code ABAQUS. They accounted for progressive damage of the material by degrading the material properties, i.e., the elastic moduli, and found that the damage induced by indentation is more localized than that for impact. Palazotto et al. [59] developed an analytical model for the quasi-static impact of composite sandwich plates. They used stress-based criteria to predict initiation of damage and degraded the stiffness of the materials to study its progression. The model accurately predicted the indentation response of the laminate panel and the core failure load. Cheon et al. [60] proposed that the progressive damage of glass fiber-reinforced composites during a Charpy impact test be simulated by deleting the fractured part of the specimen at each stage of the loading which degrades the stiffness of the composite and causes the energy to dissipate. Batra et al. [61] used constitutive relations based on a micromechanical approach to model the impact response of a carbon fiber-reinforced polymer composite plate. They implemented the material model in a user-defined subroutine in the finite element code ABAQUS and considered inertia effects in the impact simulations. They could predict accurately the contact force and the damage and failure of the plate.

Stenzler and Goulbourne [62] and Stenzler [63] performed impact tests on PMMA/Adhesive/PC laminated plates with DFA4700, IM800A and VHB4905 as adhesives. The examination of the post failure of plates revealed that the front PMMA plate had radial cracks whereas the adhesive and the PC layers remained undamaged (no failure of the adhesive interlayer or of the PC rear plate was visually noticed). Zhang et al. [64] and Tekalur et al. [65] studied the low speed impact of a PMMA plate, and reported crack patterns typical of brittle failure. Gunnarson et al. [66] performed impact tests on monolithic PC plates of various thicknesses. They reported time histories of the maximum deflection of 3.0, 4.45 and 5.85 mm thick plates for impact velocities between 10 and 50 m/s, and found that the penetration velocity for the 5.85 and 3.0 mm thick plates equaled 80 m/s and 65 m/s, respectively. Gunnarson et al. [67] conducted impact tests at velocities between 10 and 50 m/s on monolithic and laminated structures involving PMMA, PC and an adhesive. They found that PMMA (PC) has brittle (ductile) failure. Stickle and Shultz [68] simulated oblique ballistic ($\sim$750 m/s) impact on a PMMA plate, used the Johnson–Cook damage model (accounting for limited plastic deformations of PMMA), and combined it with a principal stress fracture criterion (accounting for the brittle failure (spalling) of PMMA under tensile loading) to model damage and failure of PMMA.

The mechanical behavior and failure of the PMMA, PC and TPUs (thermoplastic polyurethanes) materials taken separately can be accurately modeled for a wide range of strains, strain rates and temperatures. However, the impact response of composite PMMA/adhesive/PC laminates has mostly been studied experimentally. Here we propose a mathematical and a computational model that accounts for the complex response of the polymeric materials including effects such as strain-rate and temperature dependence, plasticity, viscosity, brittle and ductile failure and predicts the impact response and survivability of monolithic and laminated plates. The model includes brittle and ductile failure of the various constituents of the plate (failure within the materials) as well as interfacial failure on faces of the bonding interlayers (delamination). It can predict well the response of laminates to low velocity impact. It can be used to improve our understanding of their impact response, and delineate the role of the different constituents and interactions amongst them. We note that in our simulations the steel impactor is regarded as rigid and all contact surfaces as smooth.

The rest of the paper is organized as follows. Section 2 gives the mathematical model of the problem (i.e., problem description, constitutive relations for different constituents of the laminate, failure criteria for the PMMA, the PC, the TPUs, and values of material parameters). The computational model is described in Section 3, and results of several problems are presented in Section 4, and discussed in Section 5. Conclusions from this work are summarized in Section 6.

2. Mathematical model

2.1. Problem description

A schematic sketch of the problem studied is exhibited in Fig. 1. The laminated rectangular plate of sides L_1 and L_2, and made of PMMA/adhesive/PC layers is impacted at normal incidence by a slow moving steel cylinder of height h and a hemispherical nose of diameter d_0. We use rectangular Cartesian coordinate axes with origin at the centroid of the top face of the rectangular laminated plate clamped on all four edges, the positive x-axis pointing to the right and the positive z-axis pointing upwards. The thicknesses of the top PMMA, the middle adhesive and the bottom PC layers are denoted by h_1, h_2 and h_3, respectively. The mathematical model developed and the analysis technique is applicable to an arbitrary number of layers in the laminate, and their materials.

2.2. Equations of motion

We use the Lagrangian description of motion to study deformations of the laminate. Thus balance laws governing deformations of the body are:

$$\begin{aligned} &\text{mass :} && \rho J = \rho_0 \\ &\text{linear momentum :} && \rho_0 \dot{\mathbf{v}} = \hat{\nabla} \cdot \mathbf{T} \\ &\text{momentum of momentum :} && \mathbf{T} \cdot \mathbf{F}^{\mathrm{T}} = \mathbf{F} \cdot \mathbf{T}^{\mathrm{T}} \end{aligned} \tag{1}$$

Here ρ and ρ_0 are mass densities in the current and the reference configurations, respectively, $J = \det(\mathbf{F})$ is the Jacobian of the deformation, $\mathbf{F} = \partial \mathbf{x}/\partial \mathbf{X}$ is the deformation gradient that maps a material point from the reference position $\mathbf{X}$ to its current location $\mathbf{x}$, a superimposed dot indicates the material time derivative, $\mathbf{v}$ is the velocity of a material point, $\mathbf{T}$ is the first Piola–Kirchhoff stress tensor related to the Cauchy stress tensor $\boldsymbol{\sigma}$ by $\mathbf{T} = J\boldsymbol{\sigma} \cdot \mathbf{F}^{-\mathrm{T}}$, and $(\hat{\nabla})$ is the gradient operator with respect to $\mathbf{X}$.

For low impact speeds, deformations of the steel impactor are assumed to be negligible as compared to those of the composite laminate. Thus we regard the impactor as rigid. Equations governing the translational and rotational motion of the rigid impactor are:

$$\begin{aligned} &\text{translation} && \dot{\mathbf{p}} = \mathbf{f} \\ &\text{rotation} && \dot{\mathbf{H}}_C = \mathbf{M}_C \end{aligned} \tag{2}$$

Here $\mathbf{p}$ and $\mathbf{H}_C$ are the linear momentum and the moment of linear momentum (or the angular momentum) of the rigid impactor, respectively, $\mathbf{f}$ is the resultant force acting on the impactor, $\mathbf{M}_C$ is the moment of forces acting on it, and the subscript C on a quantity implies that it is calculated with respect to the center of mass C of the rigid body.

2.3. Initial, boundary and continuity conditions

We study problems with bounding surfaces of the laminate, except for the surface contacting the impactor, either clamped or free. At a clamped edge, the three displacement components are set equal to zero. At a free surface, the surface tractions vanish. The contact surface between the impactor and the laminated plate is assumed to be smooth. Thus on it the following continuity conditions are imposed.

$$\begin{aligned} &\text{normal velocity :} && [\![\dot{\mathbf{u}}]\!] \cdot \mathbf{n} = 0 \\ &\text{normal traction :} && [\![\dot{\mathbf{t}}]\!] \cdot \mathbf{n} = 0 \\ &\text{tangential traction on contact surface :} && \mathbf{t} \times \mathbf{n} = \mathbf{0} \end{aligned} \tag{3}$$

Here double brackets enclosing a variable indicate the jump in it across the contact surface, $\mathbf{n}$ is a unit normal to the contact surface, $\mathbf{u}$ is the displacement field, $\mathbf{t}$ is the traction vector, and the symbol $\times$ denotes the cross product between two vectors.

The PMMA, the PC and the adhesive are initially at rest, stress free and at the uniform temperature of 300 K. At $t = 0$, the impactor just contacts the top surface of the laminated structure.

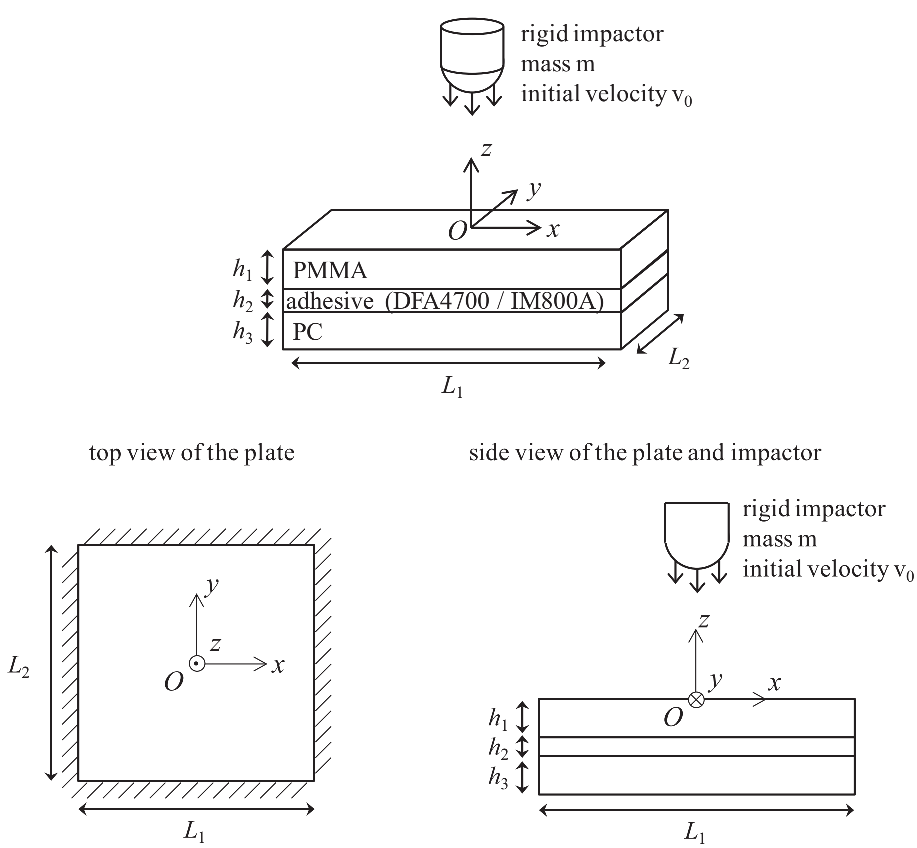

Fig. 1. Sketch of the impact problem studied.

2.4. Constitutive equations for PMMA and PC

The thermo-elasto-visco-plastic response of the PMMA and the PC polymers are modeled following the work of Mulliken and Boyce [6] with the modifications suggested by Varghese and Batra [21]. It assumes that the total Cauchy stress tensor $\boldsymbol{\sigma}$ at a material point equals the sum of contributions from three phases, namely B, α and β, i.e., $\boldsymbol{\sigma} = \boldsymbol{\sigma}_B + \boldsymbol{\sigma}_\alpha + \boldsymbol{\sigma}_\beta$. The three phases coexist at a material point and have the same value of the deformation gradient $\mathbf{F}$. The phase B behaves like a non-linear elastic Langevin spring for which

$$\boldsymbol{\sigma}_B = \frac{C_R}{3}\frac{\sqrt{N_l}}{\lambda^p}L^{-1}\left(\frac{\lambda^p}{\sqrt{N_l}}\right)\overline{\mathbf{B}}'_B \tag{4}$$

Here $\boldsymbol{\sigma}_B$ is the Cauchy stress tensor, $\overline{\mathbf{B}}'_B$ the deviatoric part of $\overline{\mathbf{B}}_B = (J)^{-2/3}\mathbf{F}\mathbf{F}^T$, $\lambda^p = \sqrt{\mathrm{tr}(\overline{\mathbf{B}}_B)/3}$ a measure of stretch, tr() the trace operator, L^{-1} the inverse of the Langevin function defined by $L(\beta) \equiv \coth\beta - 1/\beta$, N_l the limiting stretch, $C_R \equiv n_R k\theta$ the rubbery modulus, θ the temperature in Kelvin, k Boltzmann's constant, and n_R a material parameter.

The other two phases, α and β, are modeled with the same constitutive equation but with different values of material parameters. For each phase the deformation gradient $\mathbf{F}$ is decomposed into elastic and plastic parts, e.g., see Kroner [69] and Lee [70]:

$$\mathbf{F} = \mathbf{F}^e_\alpha\mathbf{F}^p_\alpha = \mathbf{F}^e_\beta\mathbf{F}^p_\beta \tag{5}$$

Neither $\mathbf{F}^e_\alpha$, $\mathbf{F}^e_\beta$ nor $\mathbf{F}^p_\alpha$, $\mathbf{F}^p_\beta$ is gradient of a vector field. The plastic deformation gradients $\mathbf{F}^p_\alpha$ and $\mathbf{F}^p_\beta$ map a material point in the reference configuration to a material point in the intermediate configuration obtained after elastically unloading the current configuration to a stress-free state.

The rate of the plastic deformation gradient in phases α and β is given by

$$\dot{\mathbf{F}}^p_\alpha = \dot{\mathbf{F}}^{e-1}_\alpha\tilde{\mathbf{D}}^p_\alpha\mathbf{F}_\alpha, \quad \dot{\mathbf{F}}^p_\beta = \dot{\mathbf{F}}^{e-1}_\beta\tilde{\mathbf{D}}^p_\beta\mathbf{F}_\beta \tag{6}$$

where $\widetilde{\mathbf{D}}^p_i$ is the plastic strain rate tensor in phase i ($i = \alpha, \beta$), and it has been assumed that the plastic spin tensors in phases α and β identically vanish. We note that $\widetilde{\mathbf{D}}^p_i$ does *not* equal the symmetric part of the velocity gradient (with respect of $\mathbf{x}$) of phase i.

The Hencky elastic strain tensors of phases α and β are defined as

$$\boldsymbol{\varepsilon}^e_\alpha = \ln\left(\sqrt{\mathbf{F}^e_\alpha\mathbf{F}^{e\,T}_\alpha}\right), \quad \boldsymbol{\varepsilon}^e_\beta = \ln\left(\sqrt{\mathbf{F}^e_\beta\mathbf{F}^{e\,T}_\beta}\right) \tag{7}$$

and the corresponding Cauchy stress tensors are given by

$$\boldsymbol{\sigma}_\alpha = \frac{1}{J}\left[2\mu_\alpha\boldsymbol{\varepsilon}^e_\alpha + \lambda_\alpha\mathrm{tr}(\boldsymbol{\varepsilon}^e_\alpha)\boldsymbol{\delta}\right], \quad \boldsymbol{\sigma}_\beta = \frac{1}{J}\left[2\mu_\beta\boldsymbol{\varepsilon}^e_\beta + \lambda_\beta\mathrm{tr}\left(\boldsymbol{\varepsilon}^e_\beta\right)\boldsymbol{\delta}\right] \tag{8}$$

where Young's moduli of phases α and β of PMMA and PC and consequently Lame's constants, λ and μ, are temperature and strain-rate dependent. They partly capture the temperature and the strain-rate dependence of the material response while Poisson's ratio is taken to be constant. Using test data given in the Appendix of Mulliken's thesis [71], we compute the temperature and the strain-rate dependence of Young's moduli of PMMA and PC. These results depicted in Figs. 2 and 3 imply that the total Young's modulus of each material increases with an increase in the strain-rate and decreases with a rise in the temperature. We note that Eq. (8) is valid for finite deformations and accounts for all geometric nonlinearities.

The plastic strain rates are assumed to be coaxial with the deviatoric Cauchy stress tensors in their respective phases, that is,

$$\tilde{\mathbf{D}}^p_\alpha = \dot{\gamma}^p_\alpha\frac{\boldsymbol{\sigma}'_\alpha}{|\boldsymbol{\sigma}'_\alpha|}, \quad \tilde{\mathbf{D}}^p_\beta = \dot{\gamma}^p_\beta\frac{\boldsymbol{\sigma}'_\beta}{|\boldsymbol{\sigma}'_\beta|} \tag{9}$$

where $\boldsymbol{\sigma}'_i$ ($i = \alpha, \beta$) is the deviatoric part of the Cauchy stress in phase i, $|\boldsymbol{\sigma}'_i| = \sqrt{\mathrm{tr}(\boldsymbol{\sigma}'_i\boldsymbol{\sigma}'_i)}$ is the magnitude of $\boldsymbol{\sigma}'_i$, and $\dot{\gamma}^p_i$ is the effective plastic strain rate in phase i. This equation implies that $\mathrm{tr}\left(\widetilde{\mathbf{D}}^p_i\right) = 0$.

The effective plastic strain rates in α and β phases are given by

$$\dot{\gamma}^p_i = \dot{\gamma}^p_{0i}\exp\left[-\frac{\Delta G_i}{k\theta}\left(1 - \frac{\tau_i}{t_i\hat{s}_i + \alpha^p_i p}\right)\right], \quad i = \alpha, \beta \tag{10}$$

where $\dot{\gamma}^p_{0i}$ ($i = \alpha, \beta$) is the pre-exponential factor, ΔG_i the activation energy, $p = -\mathrm{tr}(\boldsymbol{\sigma})/3$ the pressure, $\tau_i = \sqrt{0.5\mathrm{tr}(\boldsymbol{\sigma}'_i\boldsymbol{\sigma}'_i)}$ the equivalent shear stress, α^p_i the pressure coefficient, $\hat{s}_i = 0.077\mu_i/(1 - \nu_i)$ the athermal shear strength, ν_i Poisson's ratio, k Boltzmann's constant, and t_i an internal variable that evolves with plastic deformations. The variable $\hat{s}_i$ is function of μ_i and is, therefore, temperature and strain-rate dependent. Since no yield surface is postulated plastic deformations always occur. The evolution of internal variable t_i in phases α and β is given by

$$\dot{t}_i = \frac{h_i}{\hat{s}^0_i}\left(1 - \frac{t_i}{t^{ss}_i}\right)\dot{\gamma}^p_i, \quad i = \alpha, \beta \tag{11}$$

where t^{ss}_i and h_i are softening parameters, and $\hat{s}^0_i$ is the reference value of $\hat{s}_i$ given by the reference values of μ_i and ν_i. Eq. (11) implies that the internal variable t_i remains constant for elastic deformations.

We postulate that the energy dissipated during plastic deformations in the α and β phases is converted into heat, that is

$$\dot{Q} = J\cdot\left(\boldsymbol{\sigma}_\alpha : \tilde{\mathbf{D}}^p_\alpha + \boldsymbol{\sigma}_\beta : \tilde{\mathbf{D}}^p_\beta\right) \tag{12}$$

where $\dot{Q}$ is the heat generated per unit volume in the reference configuration. It is assumed that heating is mostly adiabatic for the impact problems studied here because there is not enough time for the heat to be conducted away, and neglecting heat conduction facilitates numerical integration of the governing differential equations. Thus the temperature rise is given by

$$\rho_0 c\dot{\theta} = \dot{Q} \tag{13}$$

where c is the specific heat of either the PMMA or the PC.

We refer the reader to Mulliken and Boyce [6] and Varghese and Batra [21] for the determination of values of material parameters from the test data for the PMMA and the PC, and for the comparison of the computed and experimental axial stress vs. axial strain curves.

2.5. Constitutive equations for the adhesives

We assume that the adhesive can be modeled as a nearly incompressible rubberlike material [63] with the elastic response given by the Ogden strain energy density function W and the viscoelastic response by the Prony series [72,73]. That is,

$$W = \sum_{n=1}^{N}\frac{\mu_n}{\alpha_n}\left(\tilde{\lambda}_1^{\alpha_n} + \tilde{\lambda}_2^{\alpha_n} + \tilde{\lambda}_3^{\alpha_n} - 3\right) + K(J - 1 - \ln(J)) \tag{14}$$

where N is an integer, $\tilde{\lambda}_i = (J)^{-1/3}\lambda_i$ is the volumetric independent principal stretch, α_n and μ_n are material parameters, and K and G, respectively, the initial bulk and the shear moduli given by $K = \frac{2(1+\nu)}{3(1-2\nu)}G$, $G = \mu = \frac{1}{2}\sum_{n=1}^{N}\alpha_n\mu_n$

The viscoelastic response of the adhesive is assumed to obey the following constitutive relation proposed by Christensen [73].

$$\dot{\boldsymbol{\sigma}}^{ve} = \sum_{m=1}^{M}2G_m\hat{\mathbf{D}}^{dev} - \sum_{m=1}^{M}2\beta_m G_m\int_{\tau=0}^{t}e^{-\beta_m(t-\tau)}\hat{\mathbf{D}}^{dev}(\tau)d\tau \tag{15}$$

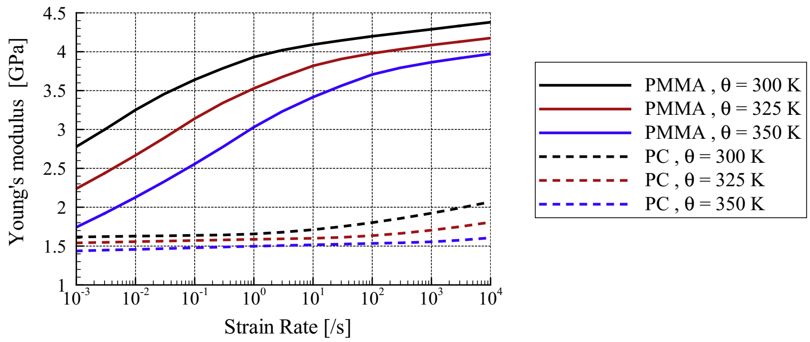

Fig. 2. Variation with the strain rate of the total Young's modulus ($E_\alpha + E_\beta$) of the PMMA and the PC.

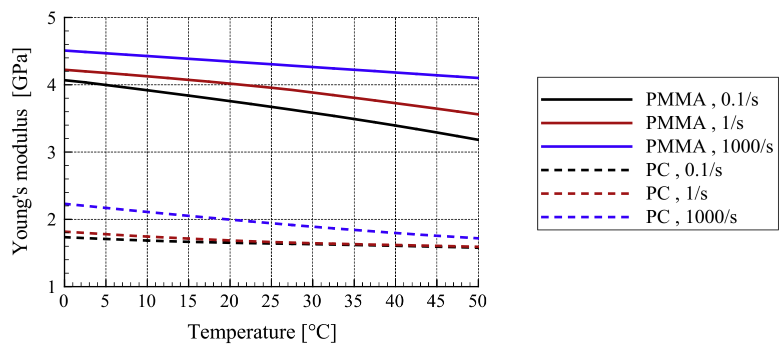

Fig. 3. Variation with the temperature of the total Young's modulus ($E_\alpha + E_\beta$) of the PMMA and the PC.

Here M is the number of terms in the summation, $\dot{\hat{\boldsymbol{\sigma}}}^{\mathrm{ve}}$ is the co-rotated rate of stress tensor (see [74] for the definition of co-rotated tensors), $\hat{\mathbf{D}}^{\mathrm{dev}}$ is the co-rotated deviatoric rate-of-deformation tensor, and G_m and β_m are material parameters representing, respectively, the shear moduli and the inverse of relaxation times. Note that there are 2 terms that determine the instantaneous elastic response of the material: Eq. (14) and the 1st term on the right-hand side of Eq. (15)

Heating of the adhesive caused by the energy dissipated due to viscous deformations is neglected since it is usually very small.

We use the test data of Stenzler [63] to find values of material parameters for the DFA4700 and the IM800A. Stenzler tested these materials in uniaxial tension at engineering strain rates of 0.01, 0.1, 1.0 and 5.0/s and in uniaxial compression at 0.001/s. The tests at 0.01/s and 0.001/s are assumed to correspond to the static nonlinear elastic response of the material and are used to find values of material parameters in the strain energy density potential (see Eq. (14)). As described below, for the DFA4700 (IM800A), two (one) terms in Eq. (14) are necessary to achieve satisfactory agreement (within 5% deviation) between the computed and the experimental axial stress–axial strain curves. Assuming that the adhesive material is incompressible, the axial stress–axial strain relation for a uniaxial tensile test conducted at constant engineering strain rate is:

$$\sigma^{\mathrm{True}} = \sum_{n=1}^{N} \mu_n \left(\exp(\alpha_n \varepsilon^{\mathrm{True}}) - \exp\left(-\frac{1}{2}\alpha_n \varepsilon^{\mathrm{True}}\right)\right) + \sum_{m=1}^{M} 3G_m \exp\left(-\frac{\exp(\varepsilon^{\mathrm{True}})}{\dot{\varepsilon}^{\mathrm{Eng}}}\beta_m\right) \times \left[\mathrm{Ei}\left(\frac{\exp(\varepsilon^{\mathrm{True}})}{\dot{\varepsilon}^{\mathrm{Eng}}}\beta_m\right) - \mathrm{Ei}\left(\frac{\beta_m}{\dot{\varepsilon}^{\mathrm{Eng}}}\right)\right] \tag{16}$$

where σ^{True} is the axial Cauchy stress, $\varepsilon^{\mathrm{True}}$ the axial logarithmic strain, $\dot{\varepsilon}^{\mathrm{Eng}}$ the constant engineering strain rate at which the test is conducted, and $\mathrm{Ei}(x) = -\int_{t=-x}^{\infty} \frac{e^{-t}}{t} dt$. The software Mathematica was used to find values of parameters in Eq. (16) so that the computed axial stress–strain curve is close to the experimental one. A single term in the series for the IM800A and two terms for the DFA4700 adhesive were found to be sufficient. The values of material parameters are given in Table 1, and the computed and the experimental stress–strain curves are depicted in Fig. 4 for the DFA4700 and in Fig. 5 for the IM800A. The deviations between the two sets of curves are listed in Table 2. We note that the two adhesives are assumed to be slightly compressible because we could not model incompressible materials in LS-DYNA. The three different values, 0.490, 0.495 and 0.498, of Poisson's ratio showed no noticeable differences among the computed results. The numerical results presented and discussed herein are obtained with Poisson's ratio = 0.498 which gives the initial bulk modulus of about 250 times the initial shear modulus. Values of Poisson's ratio greater than 0.498 significantly increase the computational cost, and were not considered. We note that only the monotonic part of the experimental axial stress–strain curve has been employed to find values of material parameters.

2.6. Failure models

We model the brittle failure of PMMA in tension by using the following maximum tensile stress based criterion proposed by Fleck et al. [47]:

$$\sigma_f = \frac{1}{\upsilon_f}\left(kT \ln\left(\frac{\dot{\varepsilon}}{\dot{\varepsilon}_0}\right) + Q_f\right) \tag{17}$$

Here $\dot{\varepsilon}$ is the effective strain rate, $\dot{\varepsilon}_0 = 1.0/\mathrm{s}$ the reference effective strain rate, k the Boltzmann constant, σ_f the tensile stress at failure, T the local temperature in Kelvin, $Q_f = 2.95 \times 10^{-19}$ J and $\upsilon_f = 2.30 \times 10^{-18}$ mm^3. These values of Q_f and υ_f correspond to 178 kJ/mol activation energy and 2.3 nm^3 activation volume and

Table 1
Values of material parameters of the DFA4700 and the IM800A adhesives.

	DFA4700		IM800A	
	Mass density (mg/mm^3)	Initial Poisson's ratio	Mass density (mg/mm^3)	Initial Poisson's ratio
	1.08	0.498	1.04	0.498
	Elastic properties (strain rate independent response) for the Ogden strain energy density W)			
n	μ_n (MPa)	α_n	μ_n (MPa)	α_n
1	0.0421	5.70	2.55	1.28
2	−4.49	−1.03		
	Viscoelastic properties (strain rate dependent response, parameters in Prony series) Shear modulus, 1/relaxation time			
m	G_m (MPa)	β_m (s^{-1})	G_m (MPa)	β_m (s^{-1})
1	2.63	3.76	0.358	0.391
2	0.563	0.139		

are comparable to the values given in [47] (54 kJ/mol activation energy and 4 nm^3 activation volume for tensile tests). According to Eq. (17) the tensile stress at failure increases with the increase in the strain rate.

A strain based failure criterion is used to model the ductile failure of the PMMA and the PC. That is, the material point is assumed to fail when the accumulated logarithmic equivalent plastic strain in either phase α or phase β reaches a critical value of 5% for the PMMA [68] and 200% for the PC [49]. We note that there are two failure criteria for the PMMA – one given by Eq. (17) for the brittle failure and the 5% plastic strain for the ductile failure.

Following the work of Richards et al. [49] the failure of the DFA4700 and the IM800A adhesives is assumed to be controlled by the maximum principal tensile stress. Folgar [75] and MacAloney et al. [76] performed quasi-static uniaxial tensile tests on the IM800A polyurethane until specimens failed. The manufacturer documentation [75] lists an ultimate elongation of 510% at failure (1.8 true strain) with 28 MPa ultimate engineering stress (170 MPa true stress) while ultimate elongations between 1400% and 1500% (2.7–2.8 true strain) were measured by MacAloney et al. [76]. The manufacturer documentation of the DFA4700 adhesive [77] lists 500% ultimate elongation with 37.9 MPa ultimate strength for a uniaxial tensile test. This corresponds to the true axial strain of 1.8 and the true axial stress of 225 MPa.

In the results presented below, it has been assumed that the DFA4700 (IM800A) fails when the maximum principal tensile stress equals 225 MPa (170 MPa).

2.7. Delamination criterion

We use the bilinear traction-separation relation, exhibited in Fig. 6, in the cohesive zone model (CZM) to simulate delamination at an interface between two distinct materials, e.g., see Gerlach et al. [78]. The ultimate displacements in modes I and II have the same value δ^f, the damage initiation displacements in modes I and II also have the same value δ^0, and we take $\delta^0 = \delta^f/2$. For mixed-mode deformations, we define $\delta_m = \sqrt{\delta_I^2 + \delta_{II}^2}$ where δ_I is the separation in the normal direction (mode I) while δ_{II} is the relative tangential displacement (mode II). The mixed-mode damage

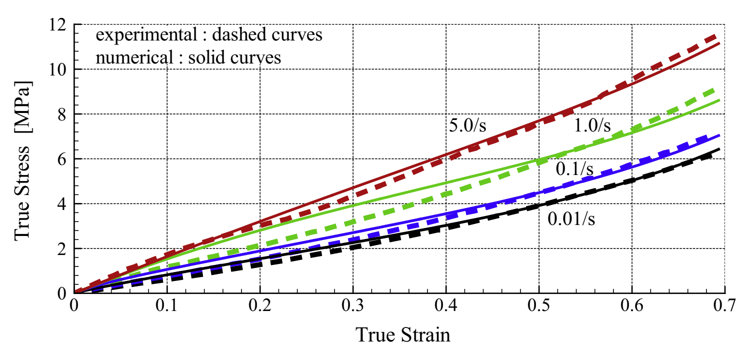

Fig. 4. Experimental and numerical results for the uniaxial tensile deformations of DFA4700 at different engineering strain rates.

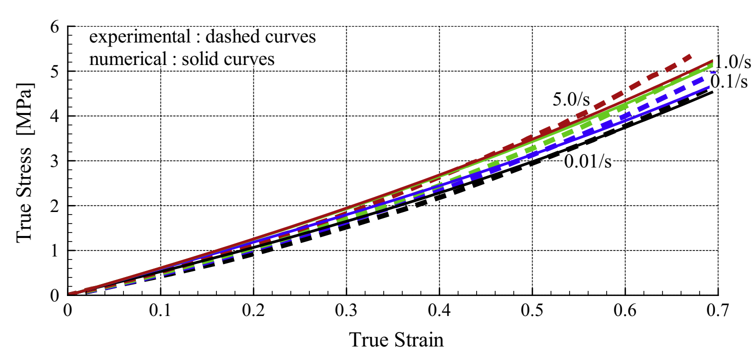

Fig. 5. Experimental and numerical results for the uniaxial tensile deformations of IM800A at different engineering strain rates.

Table 2
Deviations in L^2-norm between the predicted and the experimental responses of the DFA4700 and the IM800A subjected to axial loading.

Engineering strain rate	0.01/s	0.1/s	1.0/s	5.0/s
DFA4700	5.01%	6.50%	9.87%	3.74%
IM800A	3.97%	5.10%	5.81%	4.50%

initiation displacement is $\delta_{\mathrm{m}}^{0}=\delta^{0}$. Likewise the mixed-mode ultimate displacement is $\delta_{\mathrm{m}}^{\mathrm{f}}=\delta^{\mathrm{f}}$.

Different values of the ultimate displacement δ^{f} between 0.01 and 0.05 mm gave essentially the same values of the resisting force experienced by the impactor and the energy dissipated. Here we have assumed that $\delta^{\mathrm{f}} = 0.05$ mm. The value of the maximum traction in the CZM is determined from the value of the critical strain energy release rate (SERR) for the interface.

Pickett et al. [79] have conducted 90° peel tests on aluminum/DFA4700/PC assemblies, and reported the peel strength of 26.18 kN/m for one adhesive/PC configuration. Thus 26.2 N/mm (or equivalently 0.02618 J/mm^2) corresponds to the mode I toughness of the DFA4700/PC interface. Due to lack of data about the mode II toughness of this interface, we assume that $G_{\mathrm{II,C}} = 2G_{\mathrm{I,C}}$, which is typical for an interface between a soft polyurethane adhesive and a material with surface properties similar to those of PC. Furthermore, it is assumed that the PMMA/DFA4700 and DFA4700/PC interfaces have the same toughness values.

The manufacturer documentation for the IM800A [75] gives results of 90° peel tests of the IM800A from a glass substrate. For 80, 90, 100 and 120 °C temperature, the IM800A/glass peel force equals, respectively, 144, 155, 160 and 138 pli (pounds per linear inch). A linear fit of the peel force vs. the temperature through the first three data points gave the peel strength of 17 N/mm at 20 °C.

It was then assumed that the PMMA/IM800A and the IM800A/PC interfaces have the same properties as the IM800A/glass interface, and that $G_{\mathrm{II,C}} = 2G_{\mathrm{I,C}}$.

3. Computational model

3.1. General description

We use the commercial FE software LS-DYNA with explicit solver in which constitutive relations for the PMMA and the PC have been implemented in a user-defined subroutine written in FORTRAN. The software has in-built material model to simulate deformations of the adhesives.

For an impact problem, Khalili et al. [80] computed numerical results for different choices of the shell element, the integration scheme and the FE mesh. They found that the "unstructured" mesh gave better results in terms of convergence vs. computational cost. We also observed a similar trend (see description of the FE mesh later in this section). They also showed that assuming the impactor to be rigid reduces the computation time with minor effects on the numerical results.

As stated above, the impactor has been modeled as a rigid body translating with a uniform velocity normal to the impact surface. All contact surfaces are assumed to be frictionless. Non-interpenetration of one material into the other is satisfied by using a penalty-based contact algorithm that considers the newly formed surfaces due to the deletion of failed elements.

In LS-DYNA, the governing partial differential equations are first reduced to nonlinear and coupled ordinary differential equations (ODEs) in time by using the Galerkin approximation. The ODEs are integrated with respect to time by using the explicit conditionally stable central-difference method using the lumped mass matrix. The critical time step size equals the time taken for an elastic wave to propagate through the smallest element in the FE mesh. We set the time step size equal to a fraction of the critical time step to ensure stability of the computed solution. The effect of the time step size on the numerical solution was investigated and the time step is fixed to a value for which the numerical solution converged. Of course, each FE mesh requires a different time step size.

The FE mesh consisted of 8-node brick elements with one point integration (reduced integration) used to evaluate element matrices. Since zero energy deformation modes (or hourglass modes) can arise due to using reduced integration rule, an hourglass control algorithm was used. The suitability of this algorithm was checked with a 3D-patch test. A cube is discretized into seven irregularly shaped hexahedrons (one for each face and one for the center, see Fig. 7). The master cube is then quasi-statically deformed in uniaxial tension. Results computed with the default and the Belytschko–Bindeman formulations are shown in Fig. 8 for an isotropic elastic material with Young's modulus = 1 GPa and Poisson's ratio = 0.25. The later formulation was selected for all numerical simulations presented herein. The energy of hourglass mode deformations was found to be less than 5% of the peak strain energy of the elastic cube implying that the hourglass modes did not introduce significant errors in the numerical solution.

For the Hertz contact problem analyzed with LS-DYNA, the maximum difference between the computed and the analytical reaction force was found to be 9.1%.

For each impact problem studied in this paper, results were computed with at least two FE meshes. The FE mesh A was uniformly refined to obtain a finer mesh B having at least 30% more nodes than those in mesh A. The solution with two FE meshes was taken to have converged if the difference in two values of the reaction force, the energy dissipated and the length of the radial cracks was less than 10%. For brevity we describe here the mesh used for the impact simulations of the laminate discussed in Section 4.3 (and that gave the converged solution). For each

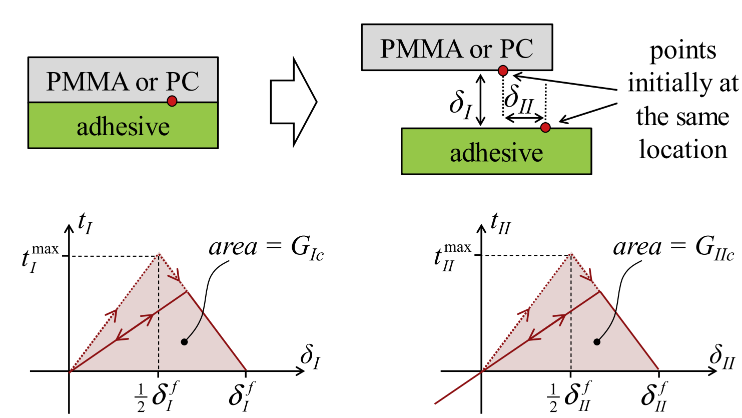

Fig. 6. Traction-separation law for delamination in mode I (bottom, left) and mode II (bottom, right).

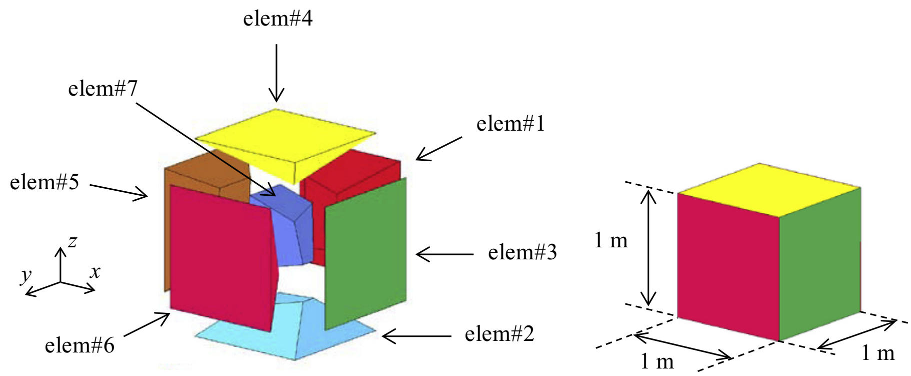

Fig. 7. Master cube formed with seven irregularly shaped hexahedrons used to check the hourglass control formulation.

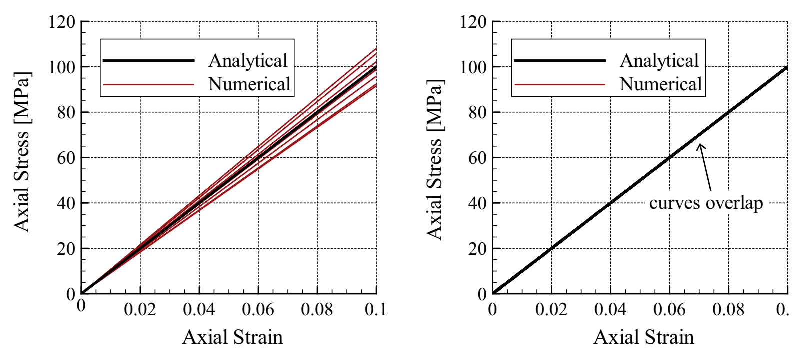

Fig. 8. Analytical stress and the computed stress in the seven hexahedron elements for the uniaxial tensile test of the master cube. Left (Right): with the default (the Belytschko–Bindeman) hourglass control.

one of the three layers the mesh in the *xy*-plane is the same. The PMMA, the interlayer and the PC are discretized, respectively, with 9, 6 and 9 uniform elements through the thickness. The CZM elements are initially flat and placed at the adhesive interfaces. The pattern of the FE mesh in the *xy*-plane is obtained by partitioning the plate along its diagonals. Then each of the four quarters of the plate is partitioned by a 10-mm radius circle centered at the point of impact. Each quarter of circumference of the circle, the part of each one of the four diagonals that are within the circle, and each edge of the plate are discretized with 55 uniform elements. The outer part of the plate diagonals, i.e., the part located more than 10-mm from the plate center, was divided into 64 segments of different lengths so that the ratio of the smallest segment – located near the circle – to the largest segment – located at the corner – equaled 15. The mesh in the impactor near the contact region was refined until the element size there was comparable to that of the elements at the plate center. The rest of the impactor was discretized with coarse elements. The FE mesh had 19,680 elements in the impactor, 209,376 elements in the PMMA and the PC layers, 139,584 elements in the adhesive interlayer, and 23,264 flat CZM elements in each interface.

The computed values of the time histories of the reaction force and the energy dissipated with perfect bonding at the PMMA/adhesive and the adhesive/PC interfaces differed from those computed considering delamination at these interfaces by less than 5%. Thus we present and discuss here only the results obtained using CZM elements at the adhesive interfaces.

3.2. Calculation of the energy dissipation

There are two main sources of energy dissipation, namely, energy dissipated due to failure of the materials (modeled with element deletion) and the energy dissipated due to inelastic deformations of the material (plasticity, viscosity, softening). When a failed element is deleted from the computational domain, its internal energy and kinetic energy are also removed. This decreases the energy of the remaining system. This change in energy is referred to as the eroded energy in LS-DYNA. The eroded energies calculated by LS-DYNA were verified using a set of simple problems for which internal and kinetic energies could be analytically determined and compared with the computed ones.

The energy dissipated due to viscous deformations of the adhesives is computed during the post-processing phase. The energy dissipated due to inelastic deformations of the PMMA and the PC is calculated for each element at each time step inside the subroutine developed for these materials. There are two sources of dissipation for these materials: energy dissipated by plastic deformations, and energy dissipated by the softening of the material attributed to decrease in Young's modulus caused by the temperature rise. This latter contribution to the energy dissipated will be referred to as "softening energy". An analogy for 1D linear elasticity and discrete stiffnesses (i.e., springs) is shown in Fig. 9. Due to stretching of the springs elastic energy is stored in the system. Subsequent heating reduces the stiffness of the material that can be simulated by removing a spring which dissipates a part of the elastic energy stored in the spring that is taken out of the system.

4. Results and discussion

4.1. Impact of monolithic PMMA plates

We first simulate the impact experiments of Zhang et al. [64] in which initially stationary and stress free clamped circular 6.35 mm thick PMMA plates of 76.2 mm diameter are impacted at normal incidence by 6.95 kg cylindrical impactor with hemispherical nose of 12.7 mm diameter translating at 0.7, 1.0, 2.0, 3.0 or 5.0 m/s. It is

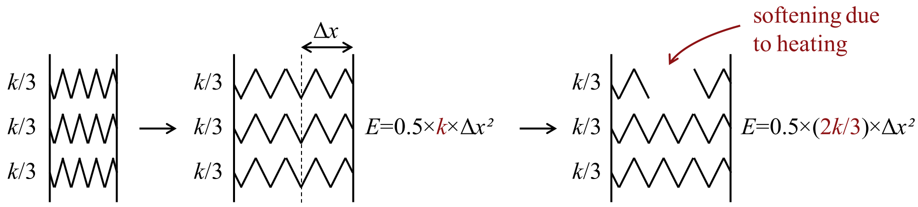

Fig. 9. Visualization of the energy dissipated due to material softening for 1D linear elastic system with a discrete spring model.

clear from the experimental and the computed fracture patterns in the plates impacted at 2.0 m/s and 3.0 m/s shown in Fig. 10 that the two sets of results agree well qualitatively. Both in tests and in simulations radial cracks but no hole developed in the plate impacted at 2.0 m/s, while the panel impacted at 3.0 m/s had radial cracks and had been perforated by the drop weight. The computed number of cracks and the crack patterns differ from those found experimentally.

4.2. Impact of monolithic PC plates

We now simulate impact experiments of Gunnarson et al. [66] in which initially stationary and stress free clamped square PC plates of side 25.4 cm and different thicknesses are impacted at normal incidence by a 104 g cylindrical steel impactor with hemispherical nose of 12.7 cm diameter. For various values of the plate thickness and the impact speed, we have compared in Table 3 the experimentally measured and the computed maximum deflections of the center of the back surface of the plates. The maximum difference in the two sets of values of 10.3% validates the mathematical model for the impact of the PC plate, at least for finding the maximum deflections. In Fig. 11 we have plotted time histories of the experimental and the computed deflections of the center of the back surface of the 5.85 and 12.32 mm thick panels impacted at various velocities. While the time of return to 0 deflection is well captured by the model for the 12.32 mm thick panel, it is not so for the 5.85 mm thick panel especially at the higher impact speed of 50.6 m/s.

The time periods of the first three modes of free vibrations of the 5.85 mm and the 12.32 mm thick clamped PC plates are 1.32, 1.60, 2.35 ms, and 0.66, 0.80, 1.12 ms, respectively. Comparing these with the time histories of the deflection of the plates shown above, we see that there is no clear correlation between the time periods of free vibration and time periods of the contact force histories.

4.3. Impact of laminated plates

We now study transient deformations of $12.7 \times 12.7\ \text{cm}^2$ clamped PMMA/Adhesive/PC laminated plate impacted at normal incidence by a 28.5 g 1-cm diameter hemispherical nosed steel cylinder at either 12 m/s or 22 m/s. Using the notation of Fig. 1, we set $h_1 = h_3 = 1.5875$ mm, and $h_2 = 0.635$ mm for the adhesive interlayer. Thus the top PMMA and the bottom PC layer have the same thickness. This configuration was used by Stenzler [63] in his experiments.

Time histories of the experimental [63] and the computed reaction force for the plates bonded with the DFA4700 and the IM800A adhesives are displayed in Fig. 12 and the deviations between the two sets of results are summarized in Table 4.

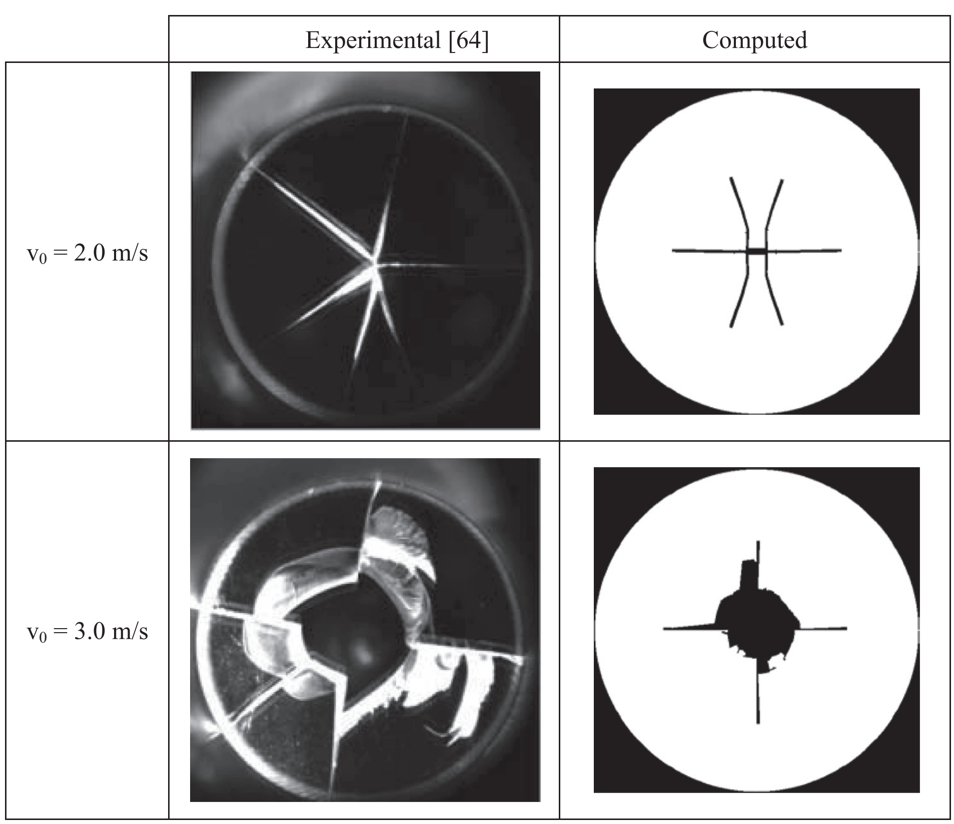

Fig. 10. Experimental and computed fracture patterns in the PMMA panels impacted at normal incidence by the rigid cylindrical impactor translating at 2.0 and 3.0 m/s.

Table 3
Comparison of the experimental and the computed maximum deflections (measured at the center of the back face of the plate) of the clamped circular PC panels.

Panel thickness (mm)	Impact velocity (m/s)				
	10	20	30	40	50
	Experimental (computed) maximum deflection (mm)				
3.00	13.2 (13.0) error: −1.5%	16.1 (17.1) error: +6.2%			
4.45	9.4 (9.0) error: −4.3%	12.9 (13.1) error: +1.6%			
5.85	6.5 (7.1) error: +9.2%	10.9 (10.2) error: −6.4%	15.2 (14.8) error: −2.6%	19.2 (19.0) error: −1.0%	22.0 (22.7) error: +3.2%
9.27			10.2 (10.4) error: +2.0%	11.3 (12.1) error: +7.1%	14.0 (14.8) error: +5.7%
12.32			6.9 (7.3) error: +5.8%	8.7 (9.6) error: +10.3%	10.7 (11.3) error: +5.6%

The time periods of the first four modes of free vibrations of the clamped laminated plates are 0.82, 0.96, and 1.34 ms (two modes) for the plate with the DFA4700 interlayer, and 0.97, 1.03, and 1.43 ms (two modes) for the IM800A adhesive. Therefore we can see that for both plates the drop in the reaction force coincides with the time period of the 1st mode, the second peak to that of the 2nd mode, and the contact termination with that of the 3rd period.

We note that the computed and the experimental time histories of the reaction force for the PMMA/DFA4700/PC laminate are close to each other except for small times for the 22 m/s impact speed and around 1.2 ms for the 12 m/s impact speed. The large local differences between the two curves give L^2-norms of deviations of $\sim$0.25. However, the numerically computed results for the PMMA/IM800A/PC laminate differ noticeably from the corresponding test findings for times beyond the time of the first peak in the reaction force. In particular the second spike in the computed reaction force at $t \approx 1.1$ ms is not found in test results. The qualitative shape of the reaction force history curve (two peaks separated by a drop) is consistent with the experimental results of Wu and Chang [57] and to the corresponding simulations by Her and Liang [81] who used ANSYS/LS-DYNA (these results were obtained for low-velocity impact of graphite/epoxy composites). Moreover we notice that the maximum value reached by the reaction force is nearly proportional to the impact velocity, which agrees with the observations of Her and Liang [81].

The characteristics of the computed crack patterns in the PMMA plate are compared with those found experimentally in Table 5. In Fig. 13 we have exhibited the crack patterns on the back surface of the PMMA plate obtained for the impact speed of 12 m/s, and in Figs. 14 and 15 we have depicted the experimental and the computed post-impact failure of the PMMA plate. These two sets of results are in good agreement with each other for the four impact scenarios studied. One can conclude from these results that the adhesive significantly affects the fracture of the PMMA plate since a change in the adhesive material noticeably alters the fracture induced in the PMMA plate. The evolution with time of the failed and hence the deleted region in the PMMA plate is also exhibited in Fig. 15. Whereas in the simulations, a cavity is developed in the PMMA plate, in tests this material is severely deformed and its mechanical properties severely degraded but it is not removed from the plate.

The energy balance at the instant of separation of the impactor from the laminates is given in Table 6. For the laminate using the DFA4700 (IM800A) this time equals $\sim$1.6 (1.8) ms and $\sim$1.4 (1.6) ms, respectively, for 12 m/s and 22 m/s impact speeds.

Values of different energies listed in the Table indicate that the main energy dissipation mechanisms are plastic deformations of the PC plate and the energy dissipated due to cracking (element deletion) of the PMMA plate. Since the PMMA is brittle, it is not surprising that its plastic deformations are negligible. The only material which partially failed in the simulations is the PMMA. The failure criteria for the other materials were not met at any point in their domains. The energy dissipated due to viscous deformations of the adhesives is small, which is consistent with the large relaxation times ($\beta^{-1} \sim 1$ s) of the DFA4700 and the IM800A as compared to the impact duration ($\sim$1 ms) considered. The delamination at the adhesive interfaces dissipated a negligible amount of energy. For the lowest impact velocity, the dissipation due to the softening of the PMMA and the PC materials contributed to about 7% of the total energy dissipation.

By comparing results depicted in Figs. 14 and 15, and considering the energy dissipated due to cracking of the PMMA plate listed in Table 6, we conclude that choosing a softer – in terms of the

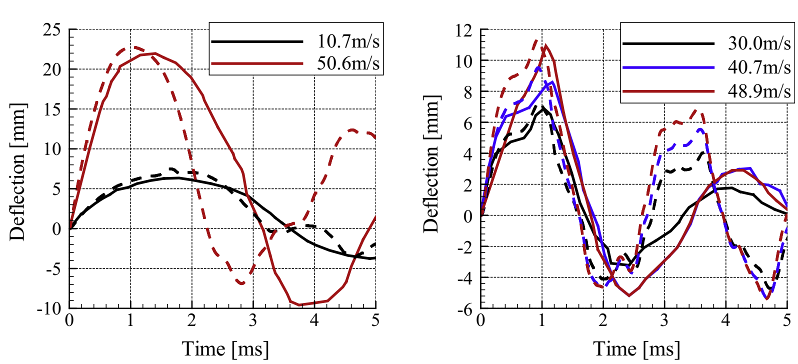

Fig. 11. Time histories of the experimental (solid curves) and the computed (dashed curves) deflections of the centers of the back face of the PC plates of thickness 5.85 mm (left) and 12.32 mm (right).

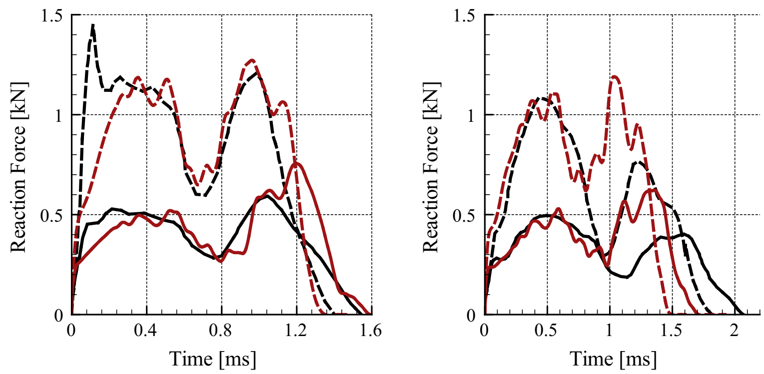

Fig. 12. Experimental (dark curves) and computed (red curves) reaction force time histories for the PMMA/DFA4700/PC (left) and the PMMA/IM800A/PC (right) plates impacted at 12 m/s (dashed curves) and 22 m/s (solid curves). (For interpretation of the references to color in this figure legend, the reader is referred to the web version of this article.)

Table 4
L^2-norm of the difference between the experimental and the computed reaction force vs. time curves.

Plate	12 m/s Impact velocity	22 m/s Impact velocity
PMMA-DFA4700-PC	0.26	0.23
PMMA-IM800A-PC	0.46	0.43

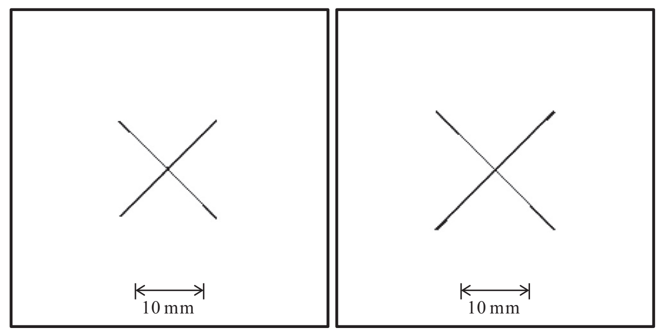

Fig. 13. Computed fracture patterns on the back surface of the PMMA plates of the PMMA/DFA4700/PC (left) and the PMMA/IM800A/PC (right) laminates for the impact speed of 12 m.

instantaneous modulus – adhesive interlayer (IM800A over DFA4700) induces longer cracks and hence larger energy dissipation due to failure of the impacted front PMMA layer but decreases the energy dissipated due to plastic deformations of the PC layer. In order to relate this to the stress wave reflections introduced by the acoustic impedance mismatch at the PMMA/adhesive and the adhesive/PC interfaces, we consider their 1-D deformations and linear elastic response. The acoustic impedance of the PMMA, DFA4700 and IM800A are, respectively, ~2.3, 0.11 and 0.077 mg mm^{-2} μs^{-1}. Therefore, in this approximation, 9% of the stress wave amplitude coming from the PMMA material and reaching the PMMA/DFA4700 interface will be transmitted to the DFA4700 interlayer, while only 6% will be transmitted for the PMMA/IM800A interface. Since the rest of the stress wave is reflected, stresses in the PMMA layer induce more damage with the IM800A adhesive. This also explains, at least partially, the lower energy dissipation in the PC layer with the IM800A rather than the DFA4700 as the adhesive. In Fig. 16, we have exhibited fringe plots of the larger of the effective plastic strain in the α and the β phases at the bottom surface of the PC plate, and in a plane orthogonal to the plate edge. It is clear that larger surface area of the PC plate is more severely plastically deformed for the DFA4700 adhesive as compared to that for the IM800A adhesive.

Time histories of the in-plane lengths of the computed cracks on the back surface of the PMMA layer in the two laminates for impact speeds of 12 and 22 m/s are plotted in Figs. 17 and 18, respectively.

The length of a radial crack increases rapidly in the early formation phase (25–35 μs for the 12 m/s impact speed, 5–15 μs for the 22 m/s impact speed) and the crack speed reaches a peak value of 1.0 mm/μs (1 km/s) for the four cases investigated. For 5000/s strain rate (which is typical for impact problems) and 300 K temperature the speed of an elastic wave in the PMMA is ~2.5 mm/μs and the Rayleigh wave speed is 1.19 mm/μs. Thus the maximum crack speed is 40% of the elastic wave speed and 84% of the Rayleigh wave speed. The crack initiation times and the corresponding values of the maximum principal stress and the strain rate at the crack initiation site are given in Table 7. The maximum principal stress in the PMMA at the time of crack initiation is essentially the same for the four cases studied, and the strain rate for the 12 m/s impact speed is about 40% less for the IM800A adhesive than that for the DFA4700 adhesive. Also, the crack initiates 4 μs earlier with the IM800A interlayer than that with the DFA4700 adhesive. For the higher impact speed of 22 m/s, the crack initiation times, the maximum principal stress and the strain rates are essentially the same for the two adhesives.

Table 5
Comparison of the experimental and the computed fracture patterns on the back surface of the PMMA plate for the PMMA/DFA4700/PC and the PMMA/IM800A/PC laminates.

Impact velocity (m/s)	Interlayer material	Experimental	Computed
12	DFA4700	No damaged material at the impact site 5 cracks, length 4–7 mm	No damaged material at the impact site 4 cracks, length 10–11 mm
12	IM800A	No damaged material at the impact site 5 cracks, length 14–17 mm	No damaged material at the impact site 4 cracks, length 12–13 mm
22	DFA4700	Diameter of damaged zone at the impact site = 5 mm 7 cracks, length 11–12 mm	Diameter of damaged zone at the impact site = 6 mm 8–9 cracks, length 10–11 mm
22	IM800A	Diameter of damaged zone at the impact site = 5 mm 6 cracks, length 22–28 mm	Diameter of damaged zone at the impact site = 7 mm 8 cracks, length 31–33 mm

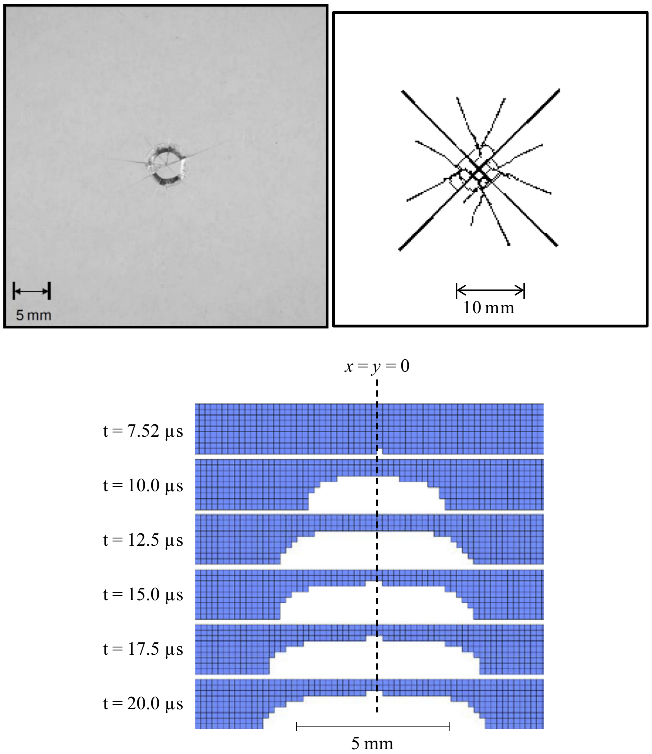

Fig. 14. Details of the experimental (left) [63] and the computed (right) fracture pattern on the back surface of the PMMA plate of the PMMA/DFA4700/PC laminate for the impact speed of 22 m/s, (bottom) the view normal to ($\mathbf{e}_x + \mathbf{e}_y$) (since the main cracks form along the diagonals) for the PMMA plate at various times.

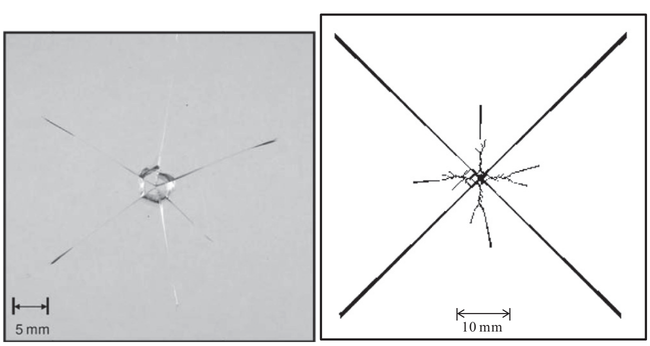

Fig. 15. (Top) Details of the experimental (left) [63] and the computed (right) fracture pattern on the back surface of the PMMA plate for the PMMA/IM800A/PC laminate for the impact speed of 22 m/s.

The reaction force, the energy dissipation, the deflection (measured at the center of the back face of the PC layer) and the in-plane extension of the cracks in the PMMA are plotted against time in Fig. 19. More than 75% of the erosion energy is not due to the elongation of radial cracks but due to the formation of the "secondary cracks", i.e., to the formation of smaller cracks and to the damage induced at the impact site (e.g., see Fig. 20 in which crack patterns at $t = 0.8$ and 1.0 ms are exhibited). This is because the number of elements that fail due to ductile failure (Johnson–Cook damage criterion) increases with time and more energy/volume is dissipated due to the ductile failure than that due to the brittle failure. We also notice that the drop in the reaction force (at ~0.7 ms) occurs when the plate deflection is the maximum. At this time, the radial cracks have reached their maximum length. There is almost no energy eroded subsequent to the reaction force decreasing to 0.65 kN at $t = \sim 0.7$ ms as shown by the eroded energy reaching a plateau between 0.65 ms and 0.90 ms. The majority of the energy erosion occurs during the spring back phase of the plate (reloading corresponding to the second peak of the reaction force, and return to the 0 deflection position).

5. Summary and discussion

We have analyzed by the FEM transient deformations of PMMA/DFA4700/PC and PMMA/IM800A/PC laminates impacted at normal incidence by a 28.5 g hemispherical nosed steel cylinder translating at 12 m/s and 22 m/s. The computed results are found to reasonably agree with the corresponding experimental ones. These simulations confirm the "sacrificial" role of the front PMMA plate. Results computed by enhancing the failure stress of the PMMA by 15% induced less damage in the impacted face of the PMMA in the PMMA/DFA4700/PC laminate but increased by 20% damage at the center of the rear face of the PC plate. Hence plastic deformations and failure of the impacted PMMA plate dissipate energy and protect the rear plate of the assembly.

In Fig. 21 are plotted the equivalent stress $\hat{\sigma} = \sqrt{\frac{3}{2}\boldsymbol{\sigma}' : \boldsymbol{\sigma}'}$ against the effective strain $\hat{\varepsilon} = \sqrt{\frac{2}{3}\boldsymbol{\varepsilon}' : \boldsymbol{\varepsilon}'}$ at the center of the back surface of the PC layer (where the damage is maximum). Here $\boldsymbol{\sigma}'$ is the deviatoric part of the Cauchy stress tensor and $\boldsymbol{\varepsilon}'$ the deviatoric part of the Hencky strain tensor. The stress–strain curves for the PMMA/DFA4700/PC and the PMMA/IM800A/PC laminates are qualitatively similar, but the times corresponding to various features of the curves and magnitudes of the stresses and strains differ quantitatively. In both cases the yield stress of PC – about 80 MPa – is reached 50 μs after contact initiation. This initial phase of elastic deformation is followed by softening of the PC material that lasts until 0.5 (0.55) ms for the laminates with the DFA4700 (IM800A) adhesive. These times correspond to the first peak in the time-history of the reaction force, see Fig. 12, and with the initiation of elastic unloading of the PC during which the effective stress drops to nearly one-fourth (one-third) of its original value for the DF4700 (IMA800A) adhesive. The subsequent increase of the contact force corresponds to the elastic re-loading of the PC material. The PC deforms then plastically until the effective strain reaches its maximum value. Then there is elastic unloading of the PC followed by an increase in the effective stress while the effective strain decreases. This corresponds to switching from tensile to compressive deformations of the PC as made clear by the two non-zero in-plane principal stresses plotted in Fig. 22, the 3rd out-of-plane principal stress is zero. The maximum effective strain at the point in the PC layer and the transition from tensile to compressive deformations occurs during the second peak of the reaction force. It is clear from these plots that the evolution of stresses and strains in the PC is unaffected by the initiation and propagation of cracks in the PMMA layer.

The dominant stress component in the adhesives at points more than 5 mm in-plane distance from the interlayer centroid is the shear stress σ_{rz}. Its time history for the two laminates is plotted in Fig. 23 for the impact speed of 22 m/s. This stress component was found to be the dominant one by examining stress components at different points on the mid-plane of the adhesive layer. Therefore, the adhesive deforms mostly in shear suggesting thereby that it is mainly loaded by the relative radial sliding of the PMMA and the PC layers. However, at the centroid of the adhesive interlayer the pressure is greater than the effective stress implying that near the center of impact the adhesive transmits normal tractions mainly due to the high value of the hydrodynamic pressure.

Table 6
Energy analysis of the impact of the laminates. Energies are given in Joules.

Adhesive material of the laminated plate			DFA4700		IM800A	
Impact velocity			12 m/s	22 m/s	12 m/s	22 m/s
Initial impactor kinetic energy			2.041	6.860	2.041	6.860
Impactor kinetic energy			1.603	5.123	1.629	4.992
Plate kinetic energy			0.185	0.264	0.179	0.357
	PMMA		0.078	0.101	0.076	0.139
	Adhesive		0.029	0.61	0.027	0.081
	PC		0.078	0.102	0.076	0.137
Elastic energy of the plate			0.109	0.336	0.092	0.471
	PMMA		0.039	0.096	0.039	0.151
	Adhesive		0.031	0.068	0.026	0.147
	PC		0.038	0.172	0.028	0.173
Dissipation by plasticity, softening and viscosity			0.133	0.894	0.111	0.789
	PMMA	Plasticity	0.000	0.003	0.000	0.001
		Softening	0.005	0.007	0.005	0.007
	Adhesive	Viscosity	0.001	0.004	0.000	0.000
	PC	Plasticity	0.121	0.871	0.102	0.771
		Softening	0.005	0.010	0.004	0.010
Dissipation due to cracking/failure			0.020	0.154	0.030	0.279
	PMMA		0.020	0.154	0.030	0.279
	Adhesive		0.000	0.000	0.000	0.000
	PC		0.000	0.000	0.000	0.000
Dissipation by delamination			0.000	0.001	0.000	0.001
	PMMA-adhesive interface		0.000	0.001	0.000	0.001
	PC-adhesive interface		0.000	0.000	0.000	0.000
Remaining energy (elastic and kinetic)			1.897	5.722	1.900	5.820
Energy dissipation			0.153	1.049	0.142	1.069
Total			2.049	6.771	2.041	6.889
Variation w.r.t. initial energy			+0.42%	−1.29%	+0.02%	+0.43%

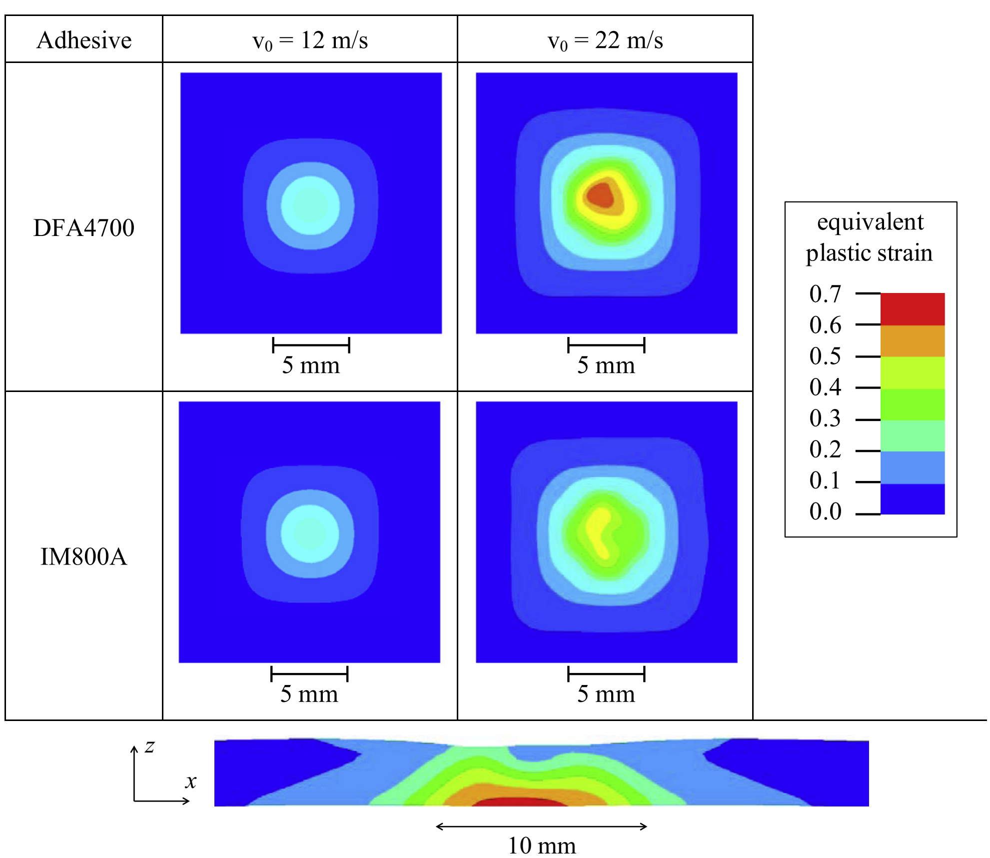

Fig. 16. For the impact of PMMA/adhesive/PC plate at 22 m/s, fringe plots in the PC layer of the computed equivalent plastic strain on the back surface (top) and for the PMMA/DFA4700/PC laminate in a plane orthogonal to the edge of the plate and passing through its center (bottom).

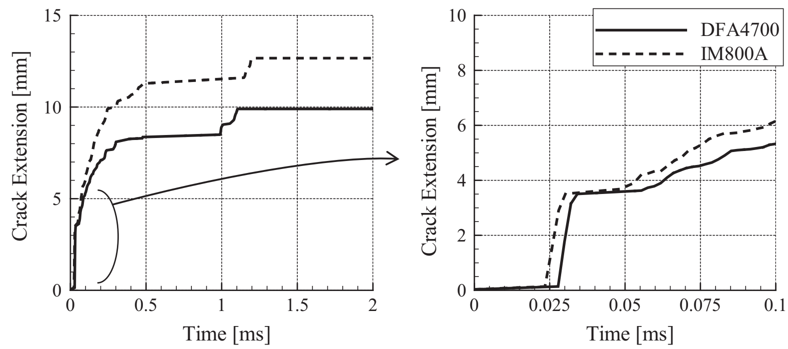

Fig. 17. Radial lengths of the cracks in the PMMA plate bonded with DFA4700 and IM800A adhesives and impacted at 12 m/s. The Fig. on the right is a magnified view of that on the left for small times.

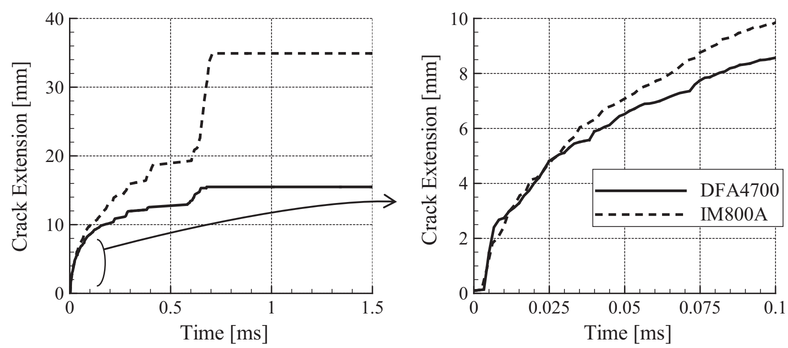

Fig. 18. Radial lengths of the cracks in the PMMA plate bonded with DFA4700 and IM800A adhesives impacted at 22 m/s. The figure on the right is a magnified view of that on the left for small times.

Table 7
Computed times of crack initiation (first element deletion), corresponding strain rates and the maximum principal stress in parentheses at the crack initiation sites. The temperature rise at these times was insignificant.

Plate	12 m/s Impact speed	22 m/s Impact speed
PMMA/DFA4700/PC	28.6 µs (1687/s, 141 MPa)	7.39 µs (2319/s, 142 MPa)
PMMA/IM800A/PC	24.4 µs (1095/s, 141 MPa)	7.51 µs (2213/s, 142 MPa)

The deformed shape of the PC layer is plotted in Fig. 24 for the 22 m/s impact speed and the PMMA/DFA4700/PC laminate. The maximum deflection, 7.57 mm, of the plate occurs at its center at 0.68 ms. It is interesting to observe that the sides of the plate initially have a negative deflection, i.e., that they have an upward displacement. This agrees with the experimental results of Stenzler [63].

The main energy dissipation mechanisms have been identified and quantified. While the viscous deformations of the adhesive interlayers do not contribute significantly to the energy dissipated during the impact process, the plastic deformations of the PC material and the cracking of the PMMA materials are responsible for more than 90% of the energy dissipated. The energy dissipated by softening of the PMMA and the PC due to temperature rise had a small contribution. The energy dissipated due to delamination at the interfaces was also miniscule.

Factors such as values of material parameters, failure criteria, delamination criteria, constitutive relations (material models) for

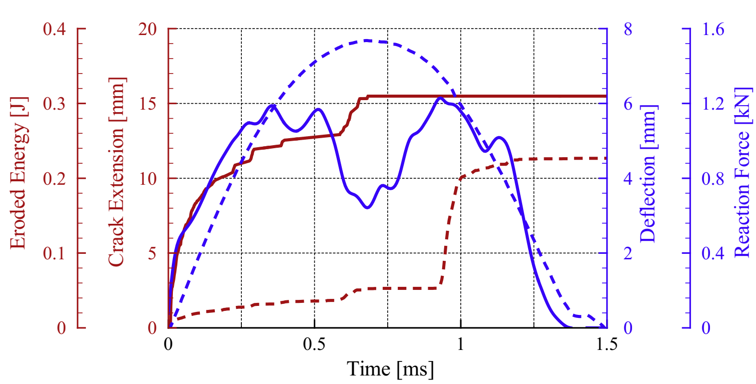

Fig. 19. Time histories of the crack length, eroded energy, reaction force, and the laminate deflection for the 22 m/s impact of the PMMA/DFA4700/PC laminate. Red curve, solid for crack extension and dashed for eroded energy; Blue curve, solid for reaction force and dashed for deflection. (For interpretation of the references to color in this figure legend, the reader is referred to the web version of this article.)

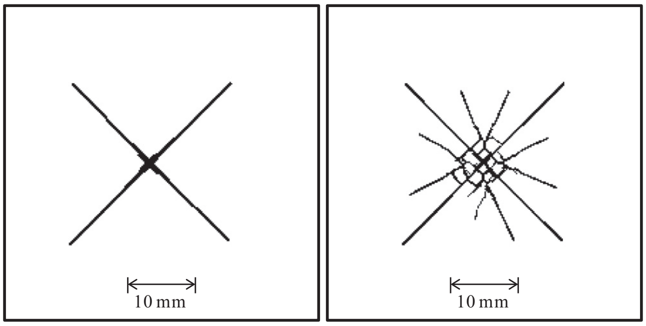

Fig. 20. Details of the crack patterns in the PMMA plate of the PMMA/DFA4700/PC laminate impacted at 22 m/s at $t = 0.8$ ms (left) and $t = 1.0$ ms (right).

the PMMA, the PC and the adhesives, and the boundary conditions affect computed results. No single paper in the literature provides a complete set of material data in order to compute results. Algorithms employed in the computational model such as the numerical integration with respect to time of the coupled nonlinear ordinary differential equations, element deletion algorithm, and the FE mesh size and the gradation of elements in the FE mesh introduce dissipation and errors in the computed solution. Of course, the test data is not necessarily exactly reproducible. It is an arduous task to quantify error introduced by each factor/parameter in a complex system such as the one analyzed here. Nevertheless the model enables one to delineate details of deformations in each component of the system, and identify dominant sources of energy dissipation.

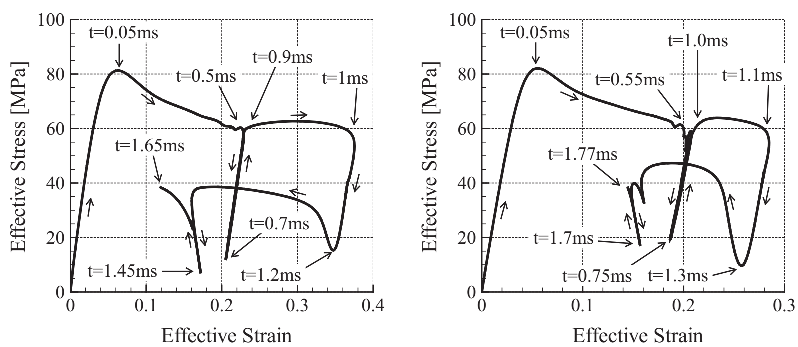

Fig. 21. Effective stress vs. effective strain curves at the point located at the center of the rear surface of the PC layer of the PMMA/DFA4700/PC (left) and PMMA/IM800A/PC (right) panels impacted at 22 m/s.

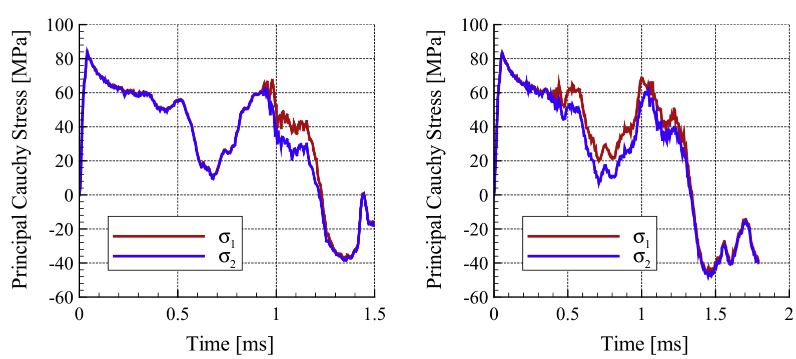

Fig. 22. Time histories of the in-plane principal stresses σ_1 and σ_2 (with $\sigma_1 \geqslant \sigma_2$) at the center of the rear surface of the PC plate of the PMMA/DFA4700/PC (left) and PMMA/IM800A/PC (right) laminates impacted at 22 m/s. The out-of-plane principal stress is zero since the surface is traction free.

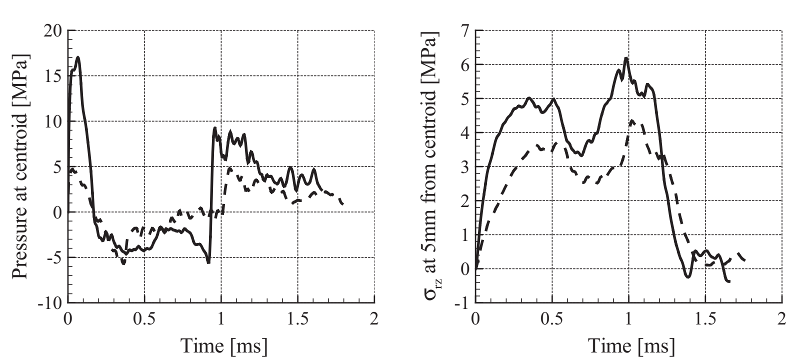

Fig. 23. Time history of the pressure at the adhesive centroid and dominant stress component at 5 mm in-plane offset from the adhesive centroid for the PMMA/DFA4700/PC (solid curves) and PMMA/IM800A/PC (dashed curves) laminates impacted at 22 m/s.

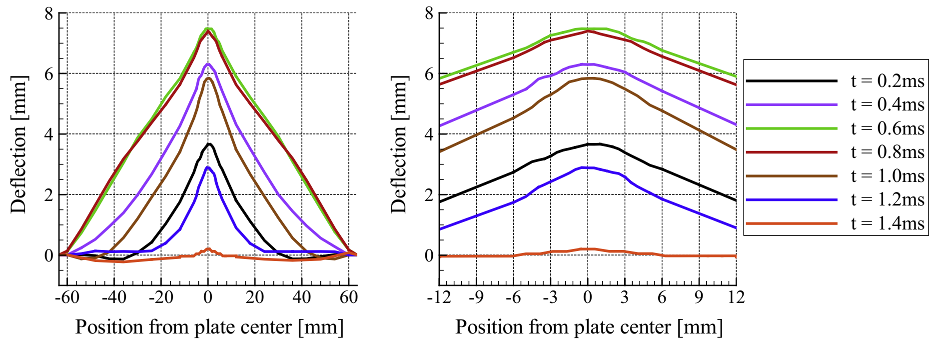

Fig. 24. Deformed shapes of the back surface of the PC plate of the PMMA/DFA4700/PC laminate impacted at 22 m/s; the right figure is a blown up view of the deformed central region of the plate.

6. Conclusions

We have developed a mathematical and a computational model to study finite transient deformations of a laminated plate impacted at normal incidence by a hemispherical nosed steel cylinder. The PMMA and the PC have been modeled as thermo-elasto-visco-plastic materials and the adhesive as a viscoelastic material. Failure of each material and of the interface between two distinct materials has been considered. Values of material parameters have been determined by using test data available in the literature. The user defined subroutine for modeling the PMMA and the PC have been implemented in the commercial software, LS-DYNA.

During the impact of the PMMA/DFA4700/PC and PMMA/IM800A/PC laminates the time history of the reaction force experienced by the impactor has two dominant peaks before dropping to zero when the impactor separates from the laminate. Whereas the computational model predicts reasonably well the portion of the reaction force time history until the first peak and the maximum deflection of the laminate, the reaction force beyond the first peak and hence the time of separation between the impactor and the laminate are not well predicted. The dominant source of energy dissipation is the plastic deformation in the PC back plate rather than the cracking of the front PMMA plate. The time of rapid drop in the reaction force corresponds to that of the maximum deflection of the plate, and at this time the radial cracks in the PMMA have reached their maximum in-plane extension. The majority of the eroded energy occurs during the rebound of the laminate to the zero deflection position. The mechanical properties of the adhesive significantly influence both the time when cracks in the PMMA initiate, the damage zone in the PMMA plate developed around the impact site, and the lengths and the number of cracks. An adhesive with a small value of instantaneous Young's modulus will result in more damage to the front layer due to the greater impedance mismatch between the PMMA and the adhesive, and will protect the rear PC layer more effectively in the sense that there will be less damage induced in it due to plastic deformations.

Acknowledgments

This research was sponsored by the Army Research Laboratory and was accomplished under Cooperative Agreement Number W911NF-06-2-0014. The views and conclusions contained in this document are those of the authors and should not be interpreted as representing the official policies, either expressed or implied, of the Army Research Laboratory or the US Government. The US Government is authorized to reproduce and distribute reprints for Government purposes notwithstanding any copyright notation hereon.

References

[1] Radin J, Goldsmith W. Normal projectile penetration and perforation of layered targets. Int J Impact Eng 1988;7:229–59.
[2] Sands J, Patel P, Dehmer P, Hsieh A. Protecting the future force: transparent materials safeguard the army's vision. AMTIAC Q 2004;8.
[3] Rabinowitz S, Ward I, Parry J. The effect of hydrostatic pressure on the shear yield behaviour of polymers. J Mater Sci 1970;5:29–39.
[4] Duckett R, Rabinowitz S, Ward I, strain-rate The. temperature and pressure dependence of yield of isotropic poly (methylmethacrylate) and poly (ethylene terephthalate). J Mater Sci 1970;5:909–15.
[5] Arruda EM, Boyce MC, Jayachandran R. Effects of strain-rate, temperature and thermomechanical coupling on the finite strain deformation of glassy-polymers. Mech Mater 1995;19:193–212.
[6] Mulliken AD, Boyce MC. Mechanics of the rate-dependent elastic–plastic deformation of glassy polymers from low to high strain rates. Int J Solids Struct 2006;43:1331–56.
[7] Siviour CR, Walley SM, Proud WG, Field JE. The high strain rate compressive behaviour of polycarbonate and polyvinylidene difluoride. Polymer 2005;46:12546–55.
[8] Moy P, Weerasooriya T, Hsieh A, Chen W. Strain rate response of a polycarbonate under uniaxial compression. In: Proceedings of the SEM conference on experimental mechanics; 2003.
[9] Richeton J, Ahzi S, Daridon L, Remond Y. A formulation of the cooperative model for the yield stress of amorphous polymers for a wide range of strain rates and temperatures. Polymer 2005;46:6035–43.
[10] Richeton J, Schlatter G, Vecchio KS, Remond Y, Ahzi S. A unified model for stiffness modulus of amorphous polymers across transition temperatures and strain rates. Polymer 2005;46:8194–201.
[11] Richeton J, Ahzi S, Vecchio KS, Jiang FC, Adharapurapu RR. Influence of temperature and strain rate on the mechanical behavior of three amorphous polymers: characterization and modeling of the compressive yield stress. Int J Solids Struct 2006;43:2318–35.
[12] Rittel D, Eliash N, Halary JL. Hysteretic heating of modified poly(methylmethacrylate). Polymer 2003;44:2817–22.
[13] Rittel D. An investigation of the heat generated during cyclic loading of two glassy polymers. Part I: Experimental. Mech Mater 2000;32:131–47.
[14] Rittel D, Rabin Y. An investigation of the heat generated during cyclic loading of two glassy polymers. Part II: Thermal analysis. Mech Mater 2000;32:149–59.
[15] Schmachtenberg E, Glissmann M, Brinkmann M. Modelling the dynamic material behaviour of thermoplastics in the FEA. J Polym Eng 2006;26:245–58.
[16] Richeton J, Ahzi S, Vecchio KS, Jiang FC, Makradi A. Modeling and validation of the large deformation inelastic response of amorphous polymers over a wide range of temperatures and strain rates. Int J Solids Struct 2007;44:7938–54.
[17] Tervoort T, Smit R, Brekelmans W, Govaert LE. A constitutive equation for the elasto-viscoplastic deformation of glassy polymers. Mech Time-Depend Mater 1997;1:269–91.
[18] Buckley CP, Jones DC. Glass–rubber constitutive model for amorphous polymers near the glass-transition. Polymer 1995;36:3301–12.
[19] Alvarado-Contreras JA, Polak MA, Penlidis A. Constitutive modeling of damage evolution in semicrystalline polyethylene. J Eng Mater Trans ASME 2010;132.
[20] Boyce MC, Parks DM, Argon AS. Large inelastic deformation of glassy-polymers. 1. Rate dependent constitutive model. Mech Mater 1988;7:15–33.
[21] Varghese AG, Batra RC. Constitutive equations for thermomechanical deformations of glassy polymers. Int J Solids Struct 2009;46:4079–94.
[22] Varghese AG, Batra RC. Strain localization in polycarbonates deformed at high strain rates. J Polym Eng 2011;31:495–519.
[23] Lajtai EZ, Carter BJ, Ayari ML. Criteria for brittle-fracture in compression. Eng Fract Mech 1990;37:59–74.
[24] Saghafi H, Ayatollahi MR, Sistaninia M. A modified MTS criterion (MMTS) for mixed-mode fracture toughness assessment of brittle materials. Mat Sci Eng A Struct 2010;527:5624–30.

[25] Seweryn A. Brittle-fracture criterion for structures with sharp notches. Eng Fract Mech 1994;47:673–81.
[26] Seweryn A, Lukaszewicz A. Verification of brittle fracture criteria for elements with V-shaped notches. Eng Fract Mech 2002;69:1487–510.
[27] Vandenberghe N, Vermorel R, Villermaux E. Star-shaped crack pattern of broken windows. Phys Rev Lett 2013;110:174302.
[28] Schultz JM. Microstructural aspects of failure in semicrystalline polymers. Polym Eng Sci 1984;24:770–85.
[29] Zairi F, Nait-Abdelaziz M, Gloaguen JM, Lefebvre JM. Modelling of the elasto-viscoplastic damage behaviour of glassy polymers. Int J Plast 2008;24:945–65.
[30] Ayatollahi MR, Aliha MRM, Hassani MM. Mixed mode brittle fracture in PMMA – an experimental study using SCB specimens. Mat Sci Eng A Struct 2006;417:348–56.
[31] Beaumont PW, Young RJ. Failure of brittle polymers by slow crack growth. J Mater Sci 1975;10:1334–42.
[32] Wada H, Seika M, Calder CA, Kennedy TC. Measurement of impact fracture-toughness for Pmma with single-point bending test using an air gun. Eng Fract Mech 1993;46:715–9.
[33] Marshall G, Williams J, Turner C. Fracture toughness and absorbed energy measurements in impact tests on brittle materials. J Mater Sci 1973;8:949–56.
[34] Moy P, Weerasooriya T, Chen W, Hsieh A. Dynamic stress-strain response and failure behavior of PMMA. In ASME; 2003.
[35] Weerasooriya T, Moy P, Casem D, Cheng M, Chen W. Fracture toughness for PMMA as a function of loading rate. In Proceedings of the 2006 SEM annual conference on experimental mechanics; June 2006. p. 5–7.
[36] Chang FC, Chu LH. Coexistence of ductile, semi-ductile, and brittle fractures of polycarbonate. J Appl Polym Sci 1992;44:1615–23.
[37] Mills N. The mechanism of brittle fracture in notched impact tests on polycarbonate. J Mater Sci 1976;11:363–75.
[38] Fraser R, Ward I. The impact fracture behaviour of notched specimens of polycarbonate. J Mater Sci 1977;12:459–68.
[39] Allen G, Morley D, Williams T. The impact strength of polycarbonate. J Mater Sci 1973;8:1449–52.
[40] Rittel D, Levin R, Maigre H. On dynamic crack initiation in polycarbonate under mixed-mode loading. Mech Res Commun 1997;24:57–64.
[41] Rittel D, Levin R. Mode-mixity and dynamic failure mode transitions in polycarbonate. Mech Mater 1998;30:197–216.
[42] Curran DR, Shockey DA, Seaman L. Dynamic fracture criteria for a polycarbonate. J Appl Phys 1973;44:4025–38.
[43] Plati E, Williams J. Effect of temperature on the impact fracture toughness of polymers. Polymer 1975;16:915–20.
[44] Plati E, Williams J. The determination of the fracture parameters for polymers in impact. Polym Eng Sci 1975;15:470–7.
[45] Adams GC, Bender RG, Crouch BA, Williams JG. Impact fracture-toughness tests on polymers. Polym Eng Sci 1990;30:241–8.
[46] Ogihara S, Ishigure T, Kobayashi A. Study on impact perforation fracture mechanism in PMMA. J Mater Sci Lett 1998;17:691–2.
[47] Fleck NA, Stronge WJ, Liu JH. High strain-rate shear response of polycarbonate and polymethyl methacrylate. Proc R Soc London A Math 1990;429:459.
[48] Livingstone I, Richards M, Clegg R. Numerical and experimental investigation of ballistic performance of transparent armour systems. In: Lightweight armour system symposium, LASS; 1999.
[49] Richards M, Clegg R, Howlett S. Ballistic performance assessment of glass laminates through experimental and numerical investigation. In: Proceedings of the 18th international symposium on ballistics; 1999. p. 1123–30.
[50] Kelly PM. Lightweight transparent armour systems for combat eyewear. In: The proceedings of the 19th international symposium of balllistics, Interlaken, Switzerland; 2001. p. 7–11.
[51] Kihara K, Isono H, Yamabe H, Sugibayashi T. A study and evaluation of the shear strength of adhesive layers subjected to impact loads. Int J Adhes Adhes 2003;23:253–9.
[52] Tsai YM, Chen YT. Transition of Hertzian fracture to flexure fracture produced in glass plates by impact. Eng Fract Mech 1983;18:1185–90.
[53] Fountzoulas C, Sands J, Gilde G, Patel P. Modeling of defects in transparent ceramics for improving military armor. In: DTIC document; 2009.
[54] Gilde GA, Patel PJ, Hsieh AJ. Improved low-cost multi-hit transparent armor. In: Army research lab aberdeen proving ground MD weapons and materials research directorate; 2006.
[55] Zee RH, Wang CJ, Mount A, Jang BZ, Hsieh CY. Ballistic response of polymer composites. Polym Compos 1991;12:196–202.
[56] Tarim N, Findik F, Uzun H. Ballistic impact performance of composite structures. Compos Struct 2002;56:13–20.
[57] Wu HYT, Chang FK. Transient dynamic analysis of laminated composite plates subjected to transverse impact. Comput Struct 1989;31:453–66.
[58] Tita V, de Carvalho J, Vandepitte D. Failure analysis of low velocity impact on thin composite laminates: experimental and numerical approaches. Compos Struct 2008;83:413–28.
[59] Palazotto AN, Herup EJ, Gummadi LNB. Finite element analysis of low-velocity impact on composite sandwich plates. Compos Struct 2000;49:209–27.
[60] Cheon SS, Lim TS, Lee DG. Impact energy absorption characteristics of glass fiber hybrid composites. Compos Struct 1999;46:267–78.
[61] Batra RC, Gopinath G, Zheng JQ. Damage and failure in low energy impact of fiber-reinforced polymeric composite laminates. Compos Struct 2012;94:540–7.
[62] Stenzler JS, Goulbourne N. Impact mechanics of transparent multi-layered polymer composites. In: Society for experimental mechanics-SEM annual conference and exposition on experimental and applied mechanics; 2009. p. V3.
[63] Stenzler JS. Impact mechanics of PMMA/PC multi-laminates with soft polymer interlayers. In: University libraries, Virginia polytechnic institute and state university, Blacksburg, VA; 2009.
[64] Zhang W, Tekalur SA, Huynh L. Impact behavior and dynamic failure of PMMA and PC plates. Dynamic behavior of materials, vol. 1. Springer; 2011. p. 93–104.
[65] Tekalur SA, Zhang W, Huynh L. Dynamic failure of monolithic and layered PMMA and PC plates; 2010.
[66] Gunnarsson CA, Ziemski B, Weerasooriya T, Moy P. Deformation and failure of polycarbonate during impact as a function of thickness. In: Proceedings of the 2009 international congress and exposition on experimental mechanics and applied mechanics; 2009.
[67] Gunnarsson CA, Weerasooriya T, Moy P. Impact response of PC/PMMA composites. Dynamic behavior of materials, vol. 1. Springer; 2011. p. 195–209.
[68] Stickle AM, Schultz PH. Exploring the role of shear in oblique impacts: a comparison of experimental and numerical results for planar targets. Int J Impact Eng 2011;38:527–34.
[69] Kröner E. Allgemeine kontinuumstheorie der versetzungen und eigenspannungen. Arch Ration Mech Anal 1959;4:273–334.
[70] Lee EH. Elastic–plastic deformation at finite strains, Stanford university, Division of engineering mechanics; 1968.
[71] Mulliken EH. Mechanics of amorphous polymers and polymer nanocomposites during high rate deformation. In: Massachusetts Institute of Technology; 2006. p. 290.
[72] Ogden RW. Non-linear elastic deformations. Courier Dover Publications; 1997.
[73] Christensen RM. A non-linear theory of viscoelasticity for application to elastomers. J Appl Mech Trans ASME 1980;47:762–8.
[74] Rankin C. Application of linear finite elements to finite strain using corotation. In: AIAA Paper AIAA-2006-1751, 47th AIAA structures, structural dynamics and materials conference; May 2006.
[75] Folgar F. Advanced aliphatic polyurethane resins for high durability and superior ballistic performance laminated glass. In: 22nd International symposium on ballistics. Vancouver BC, Canada: DESTech Publications, Inc.; 2005. p. 908–16.
[76] MacAloney N, Bujanda A, Jensen R, Goulbourne N. Viscoelastic characterization of aliphatic polyurethane interlayers In: DTIC document; 2007.
[77] A4700 Dureflex® optical aliphatic polyether polyurethane grade. In: Urethane D, editor; 2006.
[78] Gerlach S, Fiolka M, Matzenmiller A. Modelling and analysis of adhesively bonded joints with interface elements for crash analysis. In: LS-DYNA Anwenderforum, Bamberg, 2005.
[79] Pickett JE, Suriano JA, Rice ST, Li X. Weatherable multilayer articles and method for their preparation. In: Google patents; 2003.
[80] Khalili SMR, Soroush M, Davar A, Rahmani O. Finite element modeling of low-velocity impact on laminated composite plates and cylindrical shells. Compos Struct 2011;93:1363–75.
[81] Her SC, Liang YC. The finite element analysis of composite laminates and shell structures subjected to low velocity impact. Compos Struct 2004;66:277–85.